



Mineral paragenesis in Paleozoic manganese ore deposits: Depositional versus post-depositional formation processes

Hao Yan^{a,b,c}, Dao-Hui Pi^{a,*}, Shao-Yong Jiang^a, Jingwen Mao^b, Lingang Xu^d,
Xiuqing Yang^e, Weiduo Hao^c, Kaarel Mänd^{c,f}, Long Li^c, Kurt O. Konhauser^c,
Leslie J. Robbins^g

^a State Key Laboratory of Geological Processes and Mineral Resources, School of Earth Resources, China University of Geosciences, Wuhan, China

^b Institute of Earth Sciences, China University of Geosciences, Beijing, China

^c Department of Earth & Atmospheric Sciences, University of Alberta, Edmonton, AB, Canada

^d School of Earth Sciences and Resources, China University of Geosciences, Beijing, China

^e MOE Key Laboratory of Western China's Mineral Resources and Geological Engineering, School of Earth Science and Resources, Chang'an University, Xi'an, China

^f Department of Geology, University of Tartu, Tartu, Estonia

^g Department of Geology, University of Regina, Regina, SK, Canada

Received 2 October 2021; accepted in revised form 24 March 2022; Available online 29 March 2022

Abstract

Unlike modern Mn(IV)-dominated manganese nodules, ancient manganese deposits primarily contain Mn(II) (manganous) mineral phases. The general assumption is that these manganous minerals formed post-depositionally from a Mn(IV) precursor phase during diagenesis and metamorphism. However, recent studies have shown that aqueous Mn(II) may combine with either CO_2^{aq} or $\text{H}_4\text{SiO}_4^{\text{aq}}$ to nucleate and precipitate as primary manganous phases within anoxic waters. These findings thus make it difficult to assess what comprised the primary mineral assemblage of ancient Mn deposits, which in turn, has implications for understanding the redox fabric of the past marine water column. Here, we investigate the paragenesis and oxidation state of various Mn minerals (oxides, carbonates, and silicates) from the late Devonian Xialei and middle to late Permian Zunyi manganese deposits in South China. Through characterization of the micro-scale distribution, composition, and speciation of different Mn-bearing mineral phases, we provide evidence to support an oxidative mechanism during Mn cycling at the time of deposition. We document the presence of a residual oxide phase (hausmannite; Mn_3O_4) that represents a primary to early formed Mn(III)-bearing oxide preserved in Mn(II)-carbonate nodules. Additionally, we observe spherulitic textures comprised of mixed-valence Mn(II,III,IV)-silicates enclosed in diagenetic Mn(II)-carbonate laminations. Our results allow for the construction of a paragenetic model for these deposits beginning with the reduction of a primary Mn(IV) phase and the subsequent precipitation of intermediate Mn(III)-oxide or -silicate mineral phases. Following continued exposure to reducing conditions during early diagenesis, Mn(III)-oxides were then replaced by Mn(II)-carbonates. Similarly,

* Corresponding author.

E-mail address: pdaohui@163.com (D.-H. Pi).

Mn(III)-silicates were transformed into various Mn(II)-silicates during late-stage diagenesis and metamorphism. This model suggests that the accumulation of various divalent Mn mineral phases in ancient sediments may, therefore, be indicative of deposition under a water column with a sufficient oxidizing potential to induce Mn(II) oxidation.

© 2022 Elsevier Ltd. All rights reserved.

Keywords: Manganese; Carbonates; Silicates; Paragenesis; Oxidation state; Ancient sediments; South China

1. INTRODUCTION

Earth's Archean atmosphere generally lacked free oxygen (O_2). Only after two oxygenation events – the Paleoproterozoic Great Oxidation Event (GOE, 2.5–2.3 Ga) and the late Neoproterozoic (NOE, 0.8–0.5 Ga) did atmospheric O_2 finally approach levels characteristic of the modern atmosphere (Fig. 1; e.g., Lyons et al., 2014; Alcott et al., 2019; Planavsky et al., 2021). Redox-sensitive elements, such as Mn and Fe, have the potential to record paleoredox conditions and have been used to evaluate changes in the redox state of the atmosphere and oceans over the course of Earth's history (Planavsky et al., 2011; Poulton and Canfield, 2011; Johnson et al., 2013; Reinhard et al., 2013).

Manganese, the third most abundant transition metal in Earth's crust, has the highest oxidation states of all the first-row transition metals (Armstrong, 2008). Similar to Fe(II), Mn(II) is highly soluble and may be transported long distances under anoxic conditions. As such, it is expected that

hydrothermal venting associated with submarine volcanism, along with an additional minor contribution from crustal silicate weathering, would have led to a buildup of dissolved Mn(II) in the ancient oceans (Post, 1999; Maynard, 2010; Johnson et al., 2016a). To concentrate Mn into significant sedimentary deposits, Mn(II) needs to be oxidized to insoluble Mn(III) or Mn(IV) (Calvert and Pedersen, 1996). Unlike Fe(II), however, the oxidation of Mn(II) requires higher redox potentials, effectively requiring the presence of free dissolved oxygen (O_2) (Tebo et al., 2004; Morgan, 2005; Dick et al., 2009; Hansel et al., 2012; Planavsky et al., 2014; Johnson et al., 2016a; Lingappaa et al., 2019). Moreover, given strong kinetic inhibition, Mn(II) oxidation is either microbially mediated through direct enzymatic activity (Tebo et al., 2005), or catalyzed by metal oxide surfaces coupled to the reduction of O_2 or O_2 -derived species such as superoxide (Morgan, 2005; Hansel et al., 2012). Based on an earlier hypothesis of direct photosynthetic Mn(II) oxidation (Johnson et al., 2013),

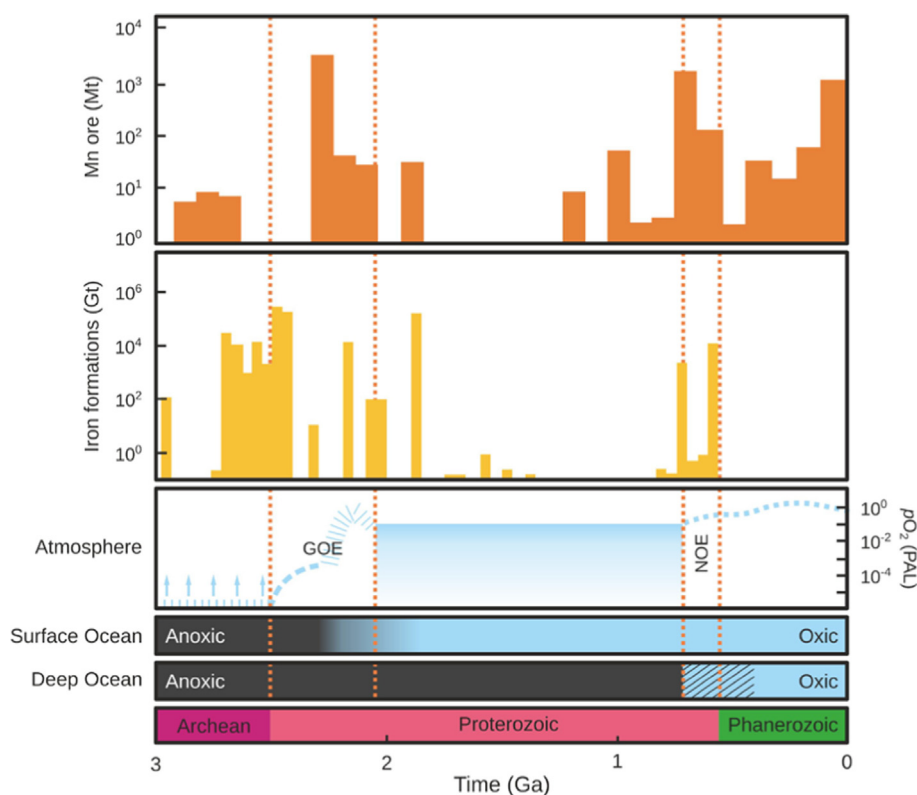


Fig. 1. Mass-age distribution of sedimentary manganese and iron ores in the context of the oxygenation of the atmosphere and hydrosphere. GOE—Great Oxidation Event; NOE—Neoproterozoic Oxidation Event; orange dashed lines bracket the duration of the oxidation events (modified from Bekker et al., 2014; Alcott et al., 2019). Black stippled lines on the “Deep Ocean” bar denote uncertainty regarding deep ocean redox in the late Neoproterozoic and early Paleozoic.

recent experiments have shown the potential for the oxidation of Mn(II) in anoxic aqueous solutions by anoxygenic phototrophs (Daye et al., 2019) or through photochemical oxidation by ultraviolet light (Anbar and Holland, 1992; Liu et al., 2020). Although plausible, these processes are inhibited by the presence of reductants (e.g., Fe(II); Planavsky et al., 2014). Furthermore, the low rates of these processes make them unlikely to be geologically significant. In this regard, Mn is rather unique in its environmental specificity for O₂ as an electron acceptor, in contrast to many of the other redox-sensitive transition metals (e.g., Fe) which can be oxidized under anoxic conditions through either a microbial pathway or with alternative oxidants such as nitrate (NO₃⁻; 10Fe²⁺ + 2NO₃⁻ + 24H₂O ↔ 10Fe(OH)₃ + N₂ + 18H⁺) (Sørensen et al., 1987). The accumulation of appreciable Mn(III,IV) oxides or complexes in the geologic record should, therefore, reflect first-order changes in the availability of O₂ and paleoenvironmental redox conditions.

The distribution of manganese metallogenesis throughout the geological record - from the Archean to recent times - is associated with the progressive oxidation of the Earth system (Fig. 1). To this end, effectively all economically exploitable Mn deposits were deposited in the aftermath of the GOE (Gutzmer and Beukes, 1996; Roy, 2000, 2006; Bekker et al., 2010; Maynard, 2010; Ossa et al., 2016). Consequently, Mn deposition within ancient sediments is generally considered to provide a window through which to evaluate the accumulation of oxygen in Earth's early atmosphere and oceans (e.g., Maynard, 2010; Johnson et al., 2016a, 2016b; Johnson, 2019). Most ancient Mn deposits, however, consist mainly of Mn(II) minerals (either as carbonates or silicates) that have experienced

both diagenesis and varying degrees of low to moderate grades of metamorphism. As such, many, if not all, minerals in Mn deposits today are the products of the combined effects of diagenesis and later alteration (Maynard, 2010; Johnson et al., 2016a; Johnson, 2019). Identifying the original precipitates of Mn deposits is, therefore, critical to understanding how Mn deposits formed and how they reflect the composition and redox state of ancient seawater. While it is difficult to pinpoint the amorphous precursor phases that originally formed in the water column, it is possible to determine the earliest formed mineral phases and their subsequent diagenetic to paragenetic sequence.

In light of geochemical similarities shared by Mn and Fe, traditional models of oxygenated waters assumed the primary Mn minerals comprised Mn(IV) oxides, e.g., pyrolusite (MnO₂) in a manner analogous with Fe(III)-oxyhydroxides characterizing the primary Fe precipitates (Maynard, 2010; Johnson et al., 2016a; Konhauser et al., 2017). In this light, the reduced Mn(II) mineral phases in the sedimentary rock record are regarded as diagenetic or metamorphic products, much the same as Fe(II) minerals that are inferred to have formed through dissimilatory Fe(III) reduction (e.g., Konhauser et al., 2005). Based on carbon isotope data, the presence of Mn(II)-carbonates, such as rhodochrosite (MnCO₃) and kutnohorite [CaMn(CO₃)₂], were attributed to the reduction of primary Mn(III/IV) oxides coupled to the oxidation of organic matter in anoxic sediment column (Fig. 2a; e.g., Calvert and Pedersen, 1996; Van Cappellen and Wang, 1996; Maynard, 2010). In addition, a distinct Mn(II,III)-silicate formation pathway has been proposed through an intermediate valence Mn(III) mineral phase: following the oxidative precipitation of Mn(IV), microbially mediated

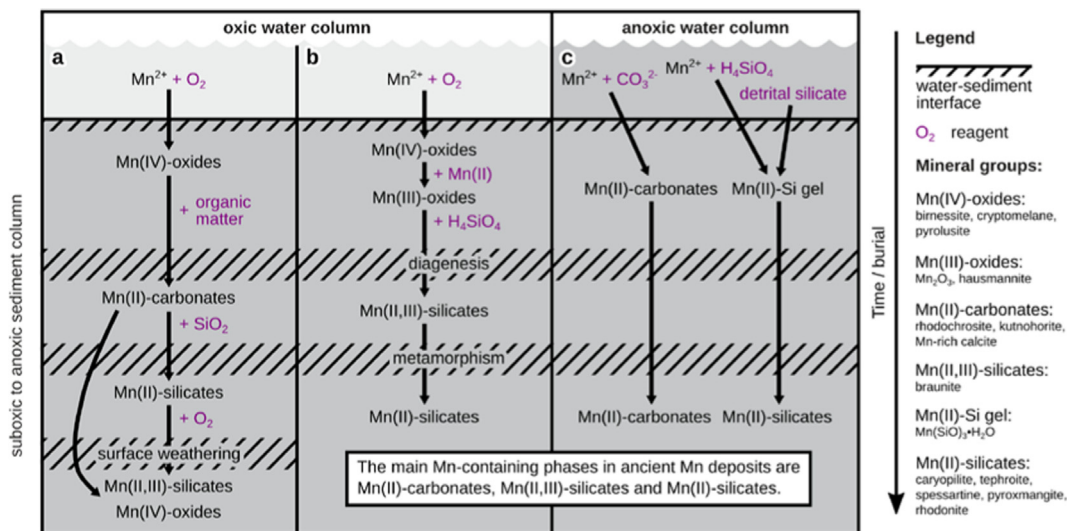


Fig. 2. Three potential pathways for the genesis of Mn minerals in ancient manganese deposits. (a) oxidation of soluble Mn(II) in an oxic water column and the subsequent transformation of Mn(IV)-oxides to Mn(II)-carbonates and Mn(II)-silicates during diagenesis in anoxic sediments and subsequent metamorphism. Later surface oxidation leading to the formation of Mn(III/IV)-oxide or -silicates is also possible (e.g., Maynard, 2010). (b) The oxidation of soluble Mn(II) to Mn(IV)-oxides under oxic water column conditions and the formation of metastable Mn(III)-oxide phases during sediment diagenesis. Later silicification of precursor Mn(III)-oxides forms Mn(III)-silicates, which are then transformed to Mn(II)-silicate during metamorphism (e.g., Johnson et al., 2016a). (c) In the absence of an oxidative mechanism in the water column, direct Mn(II)-carbonate or Mn(II)-Si gel precipitation leads to the export of Mn(II) to anoxic sediments (e.g., Herndon et al., 2018; Wittkop et al., 2020).

reduction could have produced (semi-)stable Mn(III) oxides, such as bixbyite (Mn_2O_3), that was further reduced and combined with SiO_2 during early diagenesis to form braunite ($\text{Mn(III)}_6\text{Mn(II)O}_8\text{SiO}_4$) (Robie et al., 1995; Johnson et al., 2016a). These mixed-valence silicates could then be transformed to Mn(II)-silicates, such as tephroite (Mn_2SiO_4), caryopilite ($[\text{Mn}]_3[\text{Si}_2\text{O}_5][\text{OH}]_4$), pyroxmangite ($[\text{Mn,Fe}]\text{SiO}_3$), rhodonite (MnSiO_3), and spessartine ($\text{Mn}_3\text{-Al}_2[\text{SiO}_4]_3$) during low-grade metamorphism. However, no Mn(III) oxide phases have been described in the geological record that could validate the early stages of this pathway (Fig. 2b; e.g., Johnson et al., 2016a).

Alternatively, it has been proposed that Mn(II)-carbonate phases can directly accumulate in sediments below anoxic bottom waters following nucleation on biogenic calcite in an oxygen-minimum zone because the addition of calcite triggers oversaturation with respect to Mn(II)-carbonate (Fig. 2c; Farquhar et al., 2014; Herndon et al., 2018; Wittkop et al., 2020; Gao et al., 2021; Chen et al., 2022). Similarly, Mn(II) silicates can form through the primary accumulation of an amorphous Mn(II)-Si gel under anoxic conditions before undergoing post-depositional transformations and secondary oxidation to form a variety of Mn(II,III)-silicates (Fig. 2c; Flohr and Huebner, 1992; Manceau and Gallup, 2005; Brusnitsyn, 2006; Brusnitsyn et al., 2017). This pathway is similar to that proposed for banded iron formations (BIF) in the 2.63–2.45 Ga Hamersley Group of Western Australia and the equivalent-aged Transvaal Supergroup of South Africa, where an initial Fe(II)-silicate phase, e.g., greenalite ($[\text{Fe}]_3\text{-Si}_2\text{O}_5\text{OH}_4$) has been proposed to be the primary mineral phase which was subsequently oxidized to hematite (Fe_2O_3) and magnetite (Fe_3O_4) during post-depositional processes (Rasmussen et al., 2013, 2015, 2017). However, the potential to do this over a basin scale has recently been challenged by Robbins et al. (2019), who demonstrated that given realistic hydrogeological constraints it is improbable for a BIF to have been pervasively oxidized post-depositionally. In addition, the genesis of these Mn(II, III)-silicates has also been attributed to the input, sequestration, and alteration of detrital silicates (Lenz et al., 2014; Herndon et al., 2018). None of these proposed mechanisms require Mn(IV) oxides to be present as the primary minerals and thus, they decouple the formation of appreciable Mn deposits from an oxidative mechanism. In short, the fidelity of ancient manganese deposits as reliable proxies for examining paleoenvironmental redox conditions is not settled.

Previous studies have mostly investigated the existence of primary manganese oxides in sedimentary manganese deposits by describing the whole rock geochemistry (such as C, S, Mo, and Ti isotopes), thus indirectly constraining the formation process of Mn(II)-carbonates and silicates (e.g., Maynard, 2010; Planavsky et al., 2014; Ostrander et al., 2019; Yan et al., 2020b). However, due to the diversity of minerals in manganese ores, many of which are terrigenous clastic components, the geochemical information often has multiple plausible explanations, so a variety of smaller-scale and more detailed methods such as petrography are needed for a comprehensive judgment. Neverthe-

less, only a few previous studies have identified micro-scale Mn(IV) oxide inclusions in a carbonate matrix to date (Johnson et al., 2016a; Zhang et al., 2020; Fang et al., 2020; Li et al., 2022). In addition, manganese-bearing minerals are often characterized by mixed valences [Mn(II), Mn(III), Mn(IV)], e.g., hausmannite (Mn_3O_4). Thus, determining the proportions of each valence state is critical for understanding the paragenetic sequence, as well as the local and global redox implications of Mn ore deposits. To better understand the sequence of mineralogical changes that occur during the formation of Mn deposits, from deposition through diagenesis and metamorphism, we carefully, and systematically investigated representative samples from the Late Devonian Xialei and middle-late Permian Zunyi manganese deposits, in South China. These deposits are of significant interest as they not only comprise the largest Mn deposits in China but they offer a unique opportunity to examine the various paragenetic pathways that may reflect the processes that led to the formation of significant Mn ore deposits elsewhere. Previous studies indicate that both of these deposits are characterized by a variety of Mn-bearing minerals including oxides, carbonates, and silicates, and were deposited under strongly redox-stratified waters (Chen et al., 2013; Yan et al., 2013; Wei et al., 2016) with Mn(II) sourced from seafloor hydrothermal vents (Zeng and Liu, 1999; Gao et al., 2018; Xu et al., 2021). Furthermore, the existence of parallel-to-bedding nodules and spherulite textures, mainly containing Mn-silicates, is noteworthy in the Xialei Mn deposit (Zeng and Liu, 1999).

In this work we evaluate the paragenesis of various Mn minerals using a combination of petrographic observations and scanning electron microscopy (SEM) over a range of scales. Electron probe micro-analyzer (EPMA) mapping and Laser Raman spectroscopy are further used to evaluate the chemical composition of these minerals. These petrographic and geochemical observations and measurements are then coupled to micro-scale synchrotron-based micro-X-ray adsorption near-edge structure ($\mu\text{-XANES}$) spectroscopy and X-ray photoelectron spectroscopy (XPS) analyses to characterize the redox speciation of Mn. The collective observations enable us to infer the likely primary minerals that concentrated Mn in these ancient sediments and the post-depositional processes that led to the mineralogy we observe today. Finally, we provide an assessment about whether the identified Mn-bearing minerals indeed reflect paleoseawater composition and redox conditions.

2. GEOLOGICAL SETTING

2.1. the middle to late Permian Zunyi manganese deposit

The ~ 262 Ma Zunyi manganese deposit was formed contemporaneous with the early subaqueous eruption of the Emeishan Large Igneous Province (ELIP) and it corresponds to the *J. altudaensis* biostratigraphic zone of the Capitanian Stage (Fig. 3a; e.g., Zhu et al., 2019; Yan et al., 2020a). A drowning event resulted from the subsidence of the restricted shallow water carbonate platform during the Emeishan volcanism (Fig. 3b; Sun et al., 2010;

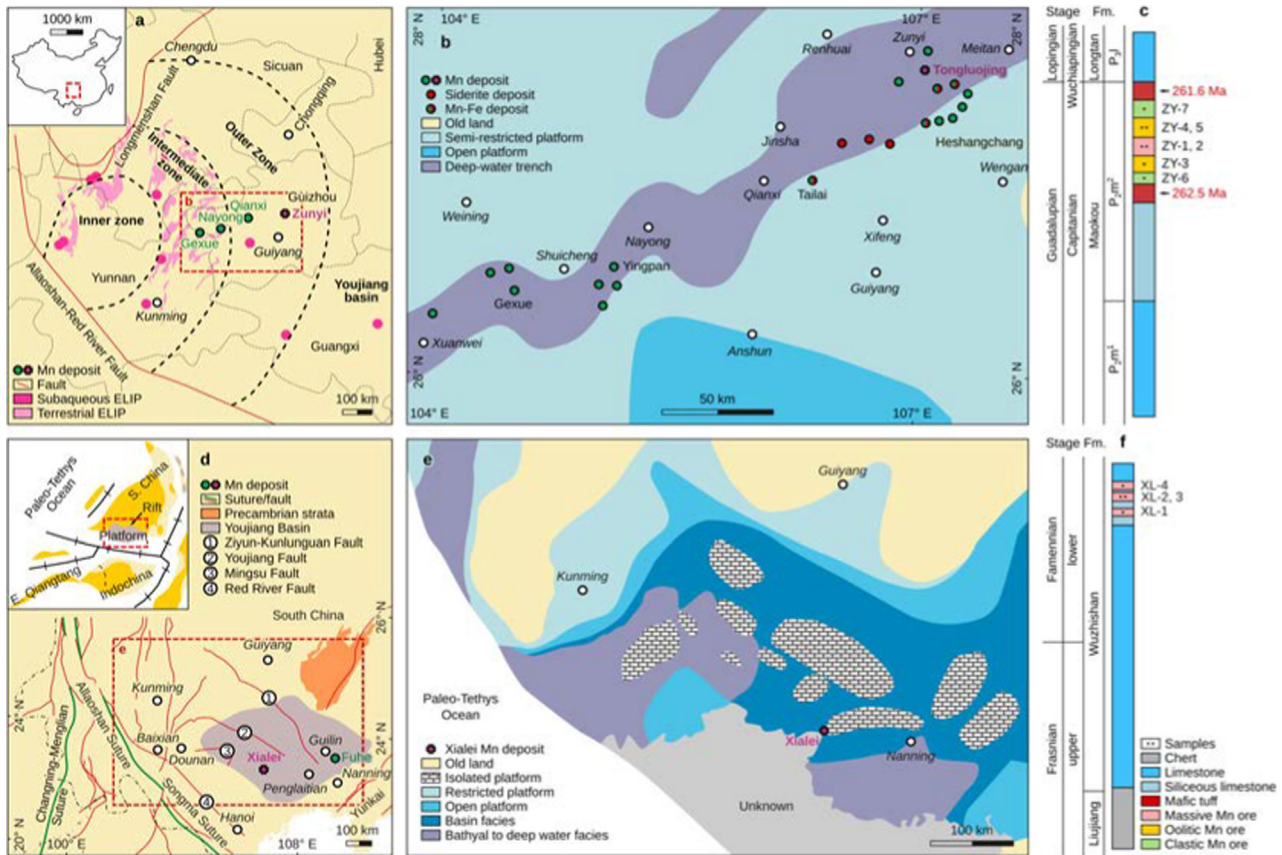


Fig. 3. (a) Simplified geological map showing the distribution of the middle-late Permian Emeishan Large Igneous Province (ELIP) and contemporaneous sedimentary manganese deposits in South China (modified from Bagherpour et al., 2018). Dashed black lines indicate the boundaries of the three Emeishan Large Igneous Province (ELIP) zones. Text labels—names of the provinces; white circles and labels in italics—respective provincial capitals; green circles—the location of studied regions of the manganese deposits reported by Liu et al. (2005) including the Gexue, Nayong, and Zunyi manganese deposits; purple polygon—Zunyi Mn deposit. Inset shows the location of the study area within China. (b) Map showing the lithofacies distribution, paleogeography, and Fe/Mn deposits formed during the middle-late Permian in central-western Guizhou (modified from Chen et al., 2003). Purple polygon is the studied Tongluojing site of the Zunyi manganese deposit. (c) Simplified stratigraphy of the Zunyi manganese deposit along with relative sampling locations. Legend in panel f. Ages from Yan et al. (2020a). (d) Geodynamic models of Late Devonian manganese mineralization in the southwestern South China Block (SCB) in the context of Palaeo-Tethyan evolution (modified from Chen et al., 2018). The simplified geological map shows the location of sedimentary Late Devonian manganese deposits in the southwestern SCB (Chen et al., 2018). Purple polygon—location of the studied Xialei mine in Daxin County, Guangxi Province. Inset details the wider tectonic situation. (e) Late Devonian paleogeography of the southwestern SCB. The lithological associations of the depositional facies are explained as follows. Open platform—limestone, marlstone, and packstone; restricted platform—marlstone-dolomite, dolomite, and limestone; isolated platform—biogenic-bioherm limestone and dolomite; bathyal-deep sea facies—chert, deep-sea chert, and mudstone; basin facies—argillaceous limestone, chert, shale, and limestone. Revised from BGMRG — Bureau of Geology and Mineral Resources of Guangxi Zhuang Autonomous Region (1985) and Chen et al. (2018). (f) Simplified stratigraphy of the Xialei manganese deposit along with relative sampling locations.

Bagherpour et al., 2018). The subsidence of the shallow water carbonate platform also resulted in the formation of uneven sinkholes and formed a series of NE trending deep water platform gullies from Zunyi and Nayong (Guizhou Province) to Geyun (Yunnan Province). These gullies could have been ~ 25–35 km in width, ~300 km in length and ~ 60 m deep, and likely controlled the formation and spatial distribution of all the middle-late Permian Mn ore deposits in South China. Owing to paleogeographic constraints, a suite of notable cherts developed along the bottom of the Mn beds in the platform gullies (Gao et al., 2018; Liu et al., 2019), forming distinctive successions compared to the shallow-water platform carbonates present on either side of the gullies. Based on pyrite sulfur isotope

ratios, Yan et al. (2013) and Wei et al. (2016) proposed that during this period the regional water column was strongly stratified, with a chemocline separating oxic shallow water from anoxic or euxinic deep water. The oxygen-depleted conditions in the bottom waters may have been the main cause for the contemporaneous end-Guadalupian mass extinction recorded in the same region; however, Yan et al. (2020a) have also pointed to an early explosive eruptive phase which could have provided a potential extinction trigger.

The Zunyi manganese deposits contain various manganese ore types, such as those characterized by massive, oolitic and clastic structures, and these have discernible vertical regularity throughout the stratigraphy of the

formation. The Oolitic Mn ore, containing 45 wt% MnO, is present in the lower ore bodies at 2 m thickness. A massive 0.5–1 m thick Mn ore layer, with the highest-grade ore (MnO ~ 65 wt%) occurs in the middle ore bodies. Clastic Mn ores in the upper ore bodies are of the lowest grade (MnO ~ 30 wt%) and about 1–2 m in thickness. The mineral composition of the Mn ores is relatively simple, with the main Mn-bearing minerals being rhodochrosite and, to a lesser degree, Mn-rich calcite. Nodules containing Mn-carbonate are common in all types of Mn ores (Fig. 3c; Gao et al., 2018).

2.2. The Late Devonian Xialei manganese deposit

The Late Devonian Xialei manganese deposit, located in Daxin County of Guangxi Province, is the largest known Mn ore reserve being mined in South China. The formation of the Mn deposit postdates the Frasnian–Famennian (F–F) mass extinction and Gondwanan glaciation (Zeng and Liu, 1999; Chen et al., 2013; Ma et al., 2016). The Xialei manganese deposit has been proposed to correspond to the opening of the Paleo-Tethys Ocean, which would have resulted in elevated fluxes of hydrothermal Mn(II) to the basin (Chen et al., 2018).

As a result of the evolution of the Palaeo-Tethys Ocean, the South China Block (SCB) was separated by the Jinshajiang, Ailaoshan, and Songma sutures from other Palaeo-Tethyan blocks, including the Indochina, Eastern Qiangtang, and Western Qiangtang blocks (Fig. 3d; Metcalfe, 2006; Deng and Wang, 2016). The Youjiang Basin covers most of the southwestern SCB and extends from southwestern China to northeastern Vietnam (Fig. 3d; Yang et al., 2012).

The Early to Middle Devonian strata in the Youjiang Basin likely represents a rift environment (Chen and Shi, 2006) which marks a large-scale regression (Zeng et al., 1993). Evidence of Devonian volcanism recorded in the SCB is likely linked to syn-depositional intraplate rifting (Du et al., 2013). In the Late Devonian (Fig. 3e), the Youjiang Basin was dominated by isolated carbonate platforms scattered across a wide basin (Ma et al., 2009). These isolated platforms consist of both limestone and dolostone and contain abundant bioherms (Ma et al., 2009). The remainder of the basin was filled with argillaceous limestone, chert, and shale. The latter may represent a deep water (>1 km) depositional environment (Chen et al., 2018). The Xialei manganese deposit occurs along the margins of the basin and is concentrated at transitional interfaces between localized uplifts and depressions in the Youjiang Basin (Fig. 3e). Based on carbonate-associated sulfate and pyrite isotopes from coeval sections, the regional water column was strongly stratified, resulting from deep water being temporarily oxygen-depleted during the F–F mass extinction. During the course of deposition, anoxic deep-water masses in the Youjiang basin gradually retracted, presumably reflecting the gradual deepening of oxygenated waters and the translation of the chemocline to greater depths (Chen et al., 2013; Yan et al., 2020b).

In the Xialei manganese deposit the ore-bearing sequence is about 10 m thick and composed of three ore

beds with two silicate interlayers (Fig. 3f). The footwall is argillaceous limestone and the hanging wall is siliceous sedimentary rocks. The mineral assemblage of the Mn ores is dominated by Mn-carbonates and Mn-silicate phases, as well as magnetite and pyrite (FeS₂). The ores have a microcrystalline texture and occur as thin, parallel or wavy beds and laminae, which are cross-cut by later stage high-temperature rhodonite veins (Zeng and Liu, 1999). From the bottom to top of each ore bed, Mn and SiO₂ contents decrease, and Fe and CaO increase. The lower part of each ore bed consists mainly of Mn-carbonate and variable amounts of Mn-silicate, whereas the upper part consists chiefly of Mn-carbonate with pyrite and is devoid of Mn-silicate. The most remarkable features of the Mn ores are their nodules, oolites, and spherulites that occur parallel to bedding and mainly contain Mn-silicate. In each Mn ore bed, these textures are concentrated in the lower part and decrease up section, coinciding with the distribution of Mn silicate minerals; these textures constitute ~ 30% of the whole ore bed weight. Previous studies have indicated that these textures were formed by precipitation and sedimentary processes at the seafloor and then reworked by gravity-flow processes forming graded beds (Zeng and Liu, 1999).

3. MATERIALS AND METHODS

Samples were collected from underground tunnels in the working Mn mines. This allowed for larger samples of fresh material to be collected for this study. Further, samples are unlikely to have experienced extensive weathering or meteoric alteration prior to collection. Seven hand samples (ZY-1 to 7) were obtained from the Zunyi Mn deposit, including two massive Mn ores, three oolitic Mn ores, and two clastic Mn ores (Fig. 3c). From the Xialei Mn deposit, four samples in total (XL-1 to 4) were collected from the lower part of each ore bed, specifically targeting the Mn-silicate nodules, oolites, and spherulites present there (Fig. 3f). A total of twenty thin sections were made from hand samples after any exposed surfaces were removed and analyzed by a range of complementary methods.

In sample XL-1 from the Xialei manganese deposit, large nodules of approximately 1 mm size were subsampled for further analysis to determine the Mn redox state (see Section 3.4). Petrographic features were imaged by backscattered electron (BSE) microscopy; images of carbon-coated samples were acquired on a JEOL JXA-8100 scanning electron microscope (SEM) at the State Key Laboratory of Geological Processes and Mineral Resources (GPMR), China University of Geosciences (Wuhan). SEM-energy dispersive X-ray spectrometry (EDS) and electron probe micro-analysis (EPMA) were subsequently used to qualitatively identify Mn-containing minerals in the studied samples and quantitatively measure their major element composition.

3.1. Electron probe micro-analysis

Mineral compositions and phase relationships were determined at GPMR using a JEOL JXA-8100 Electron

Probe Micro-Analyzer (EPMA) equipped with four wavelength-dispersive spectrometers (WDS). Samples were coated with a thin, conductive carbon film prior to analysis. The methods described in Zhang and Yang (2016) were used to minimize the difference in carbon film thickness between samples and obtain a ~ 20 nm uniform coating. Operational settings included an accelerating voltage of 15 kV, a beam current of 20 nA, a 60 ms dwell time, and a 1 μm spot size. Data were corrected on-line using a modified ZAF (atomic number, absorption, fluorescence) correction procedure. The peak counting time was 10 s for Na, Mg, Al, Si, K, Ca, Fe and 20 s for Ti and Mn. The background counting time was one-half of the peak counting time on the high- and low-energy background positions. Standards sanidine (for K), pyrope garnet (for Fe and Al), diopside (for Ca and Mg), jadeite (for Na), rhodonite (for Mn), olivine (for Si), and rutile (for Ti) were used over the course of analysis for data quality control. The EMPA was also used to map specific elements within the complex matrices of samples, complementing the sedimentological relationships observed microscopically. During the analysis, an accelerating voltage of 15 kV, a beam current of 50 nA, and a 1 μm spot size were used, along with a dwell time of 60 ms. The EMPA data are listed in (Electronic Annex Table S1).

3.2. Laser Raman spectroscopy

Mineral compositions were quantified using a Renishaw RM1000 laser Raman spectroscopic instrument housed at GPMR (Table S2). The laser was argon sourced with a wavelength of 514.5 nm and a source power of 5 mW. The charge-coupled device (CCD) detector had an area of 20 μm^2 . The spectra were recorded with counting time of 30 s over a range from 100 to 1400 cm^{-1} . A spectrograph aperture of 25 μm was chosen for the analysis. Instrumental settings were kept constant across all analyses. The Raman standard spectra for hausmannite and carboxylite were taken from the RRUFF Project website (<https://rruff.info/>; RRUFF ID R040090 and R070180, respectively).

3.3. Synchrotron-based X-ray adsorption near-edge structure spectroscopy

Synchrotron-based micro-X-ray adsorption near-edge structure (μXANES) spectra can be used to deduce the oxidation state of Mn based on comparison with reference spectra (Manceau et al., 1992, 2012; Bargar et al., 2005; Webb et al. 2005). Qualitatively, the manganese valence can be estimated from the Mn K-edge energy position (E_0), which, similar to other transition elements, shifts toward higher energies with increasing valence (Bargar et al., 2000; McKeown et al., 2003; Farges, 2005; Gunter et al., 2006). This occurs because the positive charge of the nucleus is screened by the negative charges of electrons in neutral atoms. The more electrons removed, the lower the remaining electrons' energy states become and, thus, the higher the energy of an incoming X-ray will need to

be in order to excite a core electron – meaning that the absorption edge energy increases (Gunter et al., 2006; Kelly et al., 2008). Accordingly, the position of the E_0 in Mn K-edge XANES spectroscopy – defined either as the first inflection point of Mn K-edge, the absorbance edge maximum (white line) or “halfway” up the edge – can be used as a measure of the valence of manganese (Schulze et al., 1995; Bargar et al., 2000; McKeown et al., 2003; Farges, 2005; Gunter et al., 2006). The change in an element's oxidation state is usually accompanied by a change in centro-symmetry, which will result in changes to the features of the absorption edge (Kelly et al., 2008). In addition, to more precisely and quantitatively determine the fraction of each valence in a mixed-valence system, the XANES spectra of these Mn-containing minerals were fitted to linear combinations of reference Mn species with known standard valences (Bargar et al., 2000; Manceau et al., 2012; Johnson et al., 2016b).

The speciation of Mn was determined using μXANES spectroscopy at beamline #15U (BL15U) at the Shanghai Synchrotron Radiation Facility (SSRF; Table S3). The layout of the beamline and the X-ray optics are described by Zhang et al. (2015). BL15U covers an energy range of 5–20 keV and uses an undulating X-ray source to provide photons for μXANES measurements. It employs double crystal (silicon 111) monochromators to generate monochromatic radiation focused with a Kirkpatrick-Baez mirror system. The monochromatic beam was focused down to a size of 2x2 μm . A number of slits placed downstream or upstream of the monochromator are used to define the X-ray beam profile and block unwanted X-rays. Based on EPMA maps, two areas with Mn-carbonate nodules from the Zunyi manganese deposit were selected for analysis in polished thin sections. These samples were analyzed in fluorescence mode and were placed at a 45° angle with respect to the incident X-ray beam. Vortex-90EX Si drift detectors (SDD) from SII, USA were used to detect the X-ray signals.

Ionization chambers of an appropriate gas (He) were used for monitoring the incoming and transmitting beam intensity. Manganese K-edge spectra from 6.50 keV to 6.66 keV, were collected with an energy resolution of 0.5 eV and a scanning time of 2 s. Energy calibration was monitored by use of metallic Mn (Mn foil, 6539.0 eV). All spectra were pre-edge background-subtracted and post-edge normalized with Athena from the IFEFFIT software package (Ravel and Newville, 2005).

The spectra of our samples were compared to those of fifteen pure-valence standard spectra from the database in Manceau et al. (2012), after aligning the spectra with those measured from our prepared standards, such as rhodochrosite (Supplementary Information, Fig S1, Table S3), so as to correct for laboratory-specific energy shift. The fractions of the Mn(II), Mn(III) and Mn(IV) valences in our samples were then derived using linear combination fitting analysis in the 6530–6580 eV interval by a weighted sum of these fifteen pure-valence standard spectra with the fractions of species constrained to be non-negative, called Combo method (Manceau et al., 2012) in Athena.

3.4. X-ray photoelectron spectroscopy

X-ray photoelectron spectroscopy (XPS), a non-destructive method, was used to determine and quantify the oxidation states of metals, including manganese and iron, at the near surface of materials or minerals by fitting acquired XPS spectra with those of known standards (Junta and Hochella, 1994; Jun and Martin, 2003; Biesinger et al., 2011; Ilton et al., 2016). A common approach takes advantage of the sensitivity of the bonding energy (BE) of various electron energy levels (i.e., Mn2p, Mn3p, and Mn3s) to the Mn valence state. However, it is not recommended to determine Mn oxidation states using the Mn 2p peak, as the photopeak shifts caused by differing oxidation states are too small to be assessed, especially given the sensitivity of the peak shape to differences in the Mn bonding environment (e.g., Ilton et al., 2016). Therefore, measurement of Mn 3s multiplet splitting (MS), or the shape and position of the Mn 3p photopeak, are more robust methods to estimate the valence of manganese (Cerrato et al., 2010, 2011). In contrast to the Mn2p peak, the Fe2p peak shape appears insensitive to change in Fe bonding environment over a broad range (Biesinger et al., 2011). This is similar to the Mn3p peak.

XPS measurements were performed at the Wuhan Shiyanjia Laboratory using an ESCALAB 250Xi spectrometer with a monochromatic Al K α X-ray (1486.6 eV) source

operating at 16 mA and 12.5 kV (Table S4). We specifically measured nodules with a ~ 1 mm diameter from sample XL-1 of the Xialei manganese deposits. All sample preparation occurred under atmospheric conditions. Collection efficiency was enhanced by performing 10 cycles of signal accumulation. Mn3p and Fe2p lines were measured using a 400 μ m spot size. Survey scans were recorded using a fixed pass energy (PE) of 100 eV and a step size of 0.5 eV, whereas narrow scans were collected using a fixed PE of 30 eV with a step size of 0.05 eV. Samples analyzed were charge referenced to the carbon C1s peak at 284.80 eV. Spectra were best fit, after Shirley background subtractions, by linear least squares using the Avantage software package. A least-squares Gaussian-Lorentzian algorithm was then employed for curve fitting of samples based on the shape and position of the Mn(II)O, Mn(III) $_2$ O $_3$, and Mn(IV)O $_2$ reference standards from the Thermo Scientific XPS Simplified open database (<https://xpssimplified.com/periodictable.php>).

4. RESULTS

4.1. Middle to late Permian Zunyi Mn deposit

Generally, owing to kinetic effects, chemical reactions in sedimentary systems may remain incomplete at low temperatures and numerous protolith relics may remain, making it

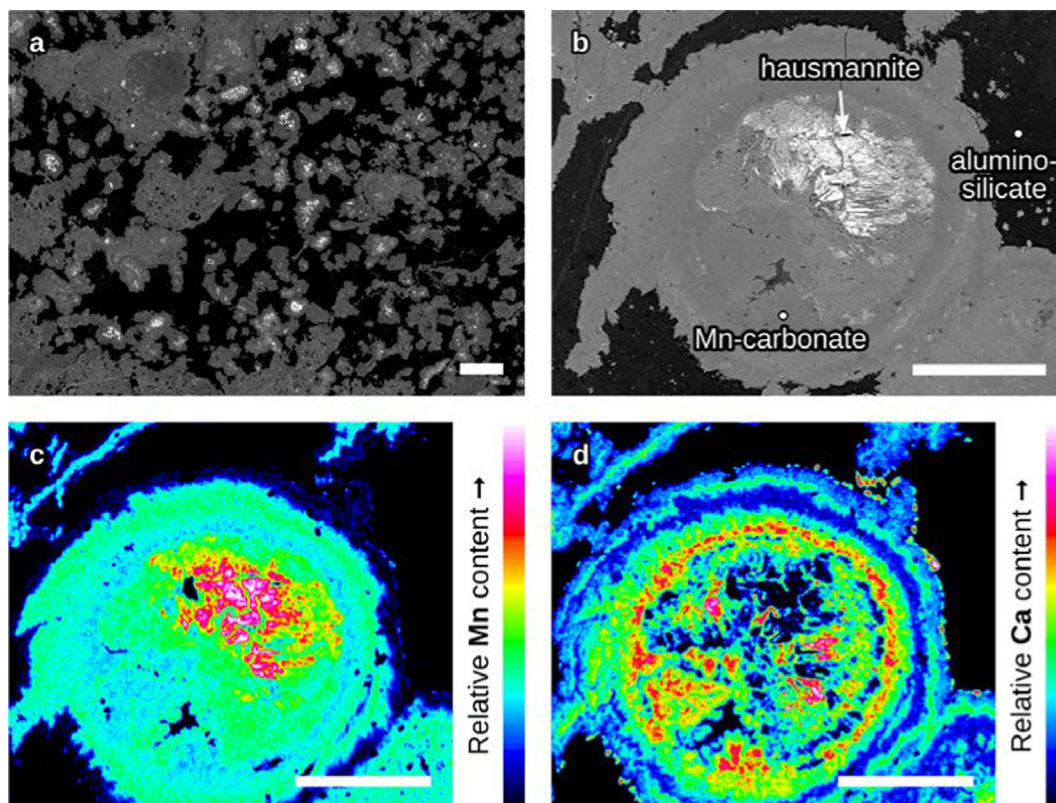


Fig. 4. (a) Back-scattered electron (BSE)-SEM images of the Zunyi manganese deposit sample Zunyi-1 showing Mn-oxide phases (white) as inclusions or unreacted residues in Ca-MnCO $_3$ nodules (dark grey). (b-d) BSE-SEM image, and EPMA Mn mapping, and EPMA Ca mapping, respectively, of a Mn-carbonate nodule that displays a typically diagenetic band structure of concentric rings around an internal Mn oxide mineral. Scale bars represent 100 μ m.

theoretically possible to trace the entire succession of phase transformation. In the Zunyi manganese deposit, such residual features were mainly found in the massive Mn ores, samples ZY-1 and 2.

In the SEM-BSE images (Fig. 4a, 4b) the “black” or darkest colored minerals in the Zunyi manganese deposit represent aluminosilicate minerals, whereas the “dark grey” nodules represent a Mn(II)-carbonate mineral. Based on the relative Ca abundance by EPMA (Table S1) and EDS measurement (Fig. S2), the composition approximates kutnohorite, rather than pure rhodochrosite.

The EPMA and EDS results (Fig. S2, Table S1) suggest that the “white” and “light grey” phases are both hausmannite based on a mixed valence Mn(II,III) oxide. This is also corroborated by laser Raman spectroscopy analyses which produce a similar spectrogram to the hausmannite standard (Fig. 5f, Table S2). While these two mineral phases are both crystalline and do not show fibrous structures related to supergene alteration by oxidizing fluids, the “light grey” phase also frequently appears fuzzy and soft, whereas the “white” mineral has a hard, mineralized texture (Figs. 5a, 5b, S3a, S4a). In EPMA elemental maps, the Mn concentrations differ between these two phases (Figs. 5c, S3d, S4c), and only “light grey” Mn oxides contain appreciable chloride (Cl) (Figs. 5e, S3d, S4e). This is especially notable in Fig. S3d where Cl is present in concentrations up to ~ 13% (Table S1). We also note the presence of hausmannite as inclusions in kutnohorite nodules (Fig. 4a, 4b, 5a, S4a). The latter is identified in elemental maps as the Ca-rich phase. In Figs. 5d, S4d, there are many Ca-bearing veinlets that cross-cut hausmannite, which suggests that the Mn-oxides were formed prior to the

Table 1

The energy positions of the absorbance maxima from standard spectra from Manceau et al., (2012) and this study.

Group	Valence state	Absorbance Maximum Position
Pure-valance standards from Manceau et al., (2012)		
Pyrolusite (β -MnO ₂)	4	6560.210
Ca ₂ Mn ₃ O ₈		6562.350
KBi		6561.770
Ramsdellite (MnO ₂)		6561.270
Groutite (α -MnOOH)	3	6557.270
Feitknechtite (β -MnOOH)		6560.090
Manganite (γ -MnOOH)		6560.710
Mn ₂ O ₃		6558.810
Pyroxmangite [(Mn,Fe)SiO ₃]	2	6551.950
Rhodochrosite (MnCO ₃)		6550.350
Fungi (Mn ₂ + -sorbed fungi)		6552.590
Hureaulite {Mn ₅ (PO ₄)[PO ₃ (OH)] ₂ -4H ₂ O}		6552.770
Manganosite (MnO)		6554.870
Tephroite (Mn ₂ SiO ₄)		6553.430
MnSO ₄ s		6552.870
Standards from this study		
MnO ₂	4	6560.564
Mn ₂ O ₃	3	6558.824
Mn ₃ O ₄	2(1/3) and 3(2/3)	6558.384
MnCO ₃	2	6550.564

Table 2

The energy positions of the absorbance maxima and linear combinations fitting results of each sample spectra in Fig. 5 and S3 using standard spectra from Manceau et al., (2012). Check Table S3 for detail fraction of each pure-valence standard.

Group	Absorbance Maximum Position	Mn(IV) fraction	Mn (III) fraction	Mn(II) fraction	Average Mn valence
spot 1	6558.784	0.115	0.570	0.316	2.802
spot 2	6558.784	0.114	0.571	0.315	2.799
spot 3	6558.764	0.119	0.572	0.314	2.820
spot 4	6558.724	0.111	0.578	0.311	2.800
spot 5	6558.784	0.126	0.556	0.317	2.806
spot 6	6558.724	0.154	0.515	0.330	2.821
spot 7	6558.224	0.028	0.557	0.413	2.609
spot 8	6558.144	0.028	0.554	0.419	2.612
spot 9	6558.324	0.033	0.570	0.397	2.636
spot 10	6558.304	0.031	0.568	0.401	2.630
spot 11	6558.244	0.021	0.567	0.412	2.609
spot 12	6558.184	0.030	0.552	0.418	2.612
spot 13	6550.704	-	0.104	0.892	2.096
spot 14	6550.764	-	0.097	0.882	2.055
spot 15	6550.724	-	0.118	0.879	2.112

early-diagenetic Ca-Mn-carbonates. In Fig. 4b-d, a diagenetic band structure comprised of concentric rings around the Mn oxide mineral is present, also suggesting that hausmannite pre-dates the diagenetically formed Mn-carbonate rings.

In this study, the E_0 for each sample and standard measured by the absorbance edge maximum are listed in Tables 1 and 2. As the energy position of the XANES absorbance maximum increases with the higher oxidation state, the range of maxima for these standards (in eV) from the database in Manceau et al. (2012) and our study increase from about 6550 ~ 6554 < 6557 ~ 6560 < 6560 ~ 6562, and correspond to oxidation states of 2, 3 to 4, respectively. The results of linear combination fitting of the fifteen pure-valence standards from the database in Manceau et al. (2012) to our samples are listed in Table 2 and S3, and the reproductions of our samples are shown in Fig. 5g and S4f.

The energy position of the absorbance maximum (E_0) in “white” Mn-oxides is generally 6558.7 eV, and the “light grey” Mn-oxide phases show a slight decrease in E_0 that eventually obtains a value of 6558.2 eV. This behavior can qualitatively suggest that the average oxidation state of these two solid-phase Mn phases both fall into the range of valence state 2–3 because of the rather small energy shift (0.5 eV) relative to the large energy variability from the same valence group. However, there is some change in the shape of the XANES spectra between these two phases. The “white” Mn-oxide spectra are more similar to those of our prepared standard hausmannite, while the spectra of the “light grey” Mn-oxides have pronounced shoulder at

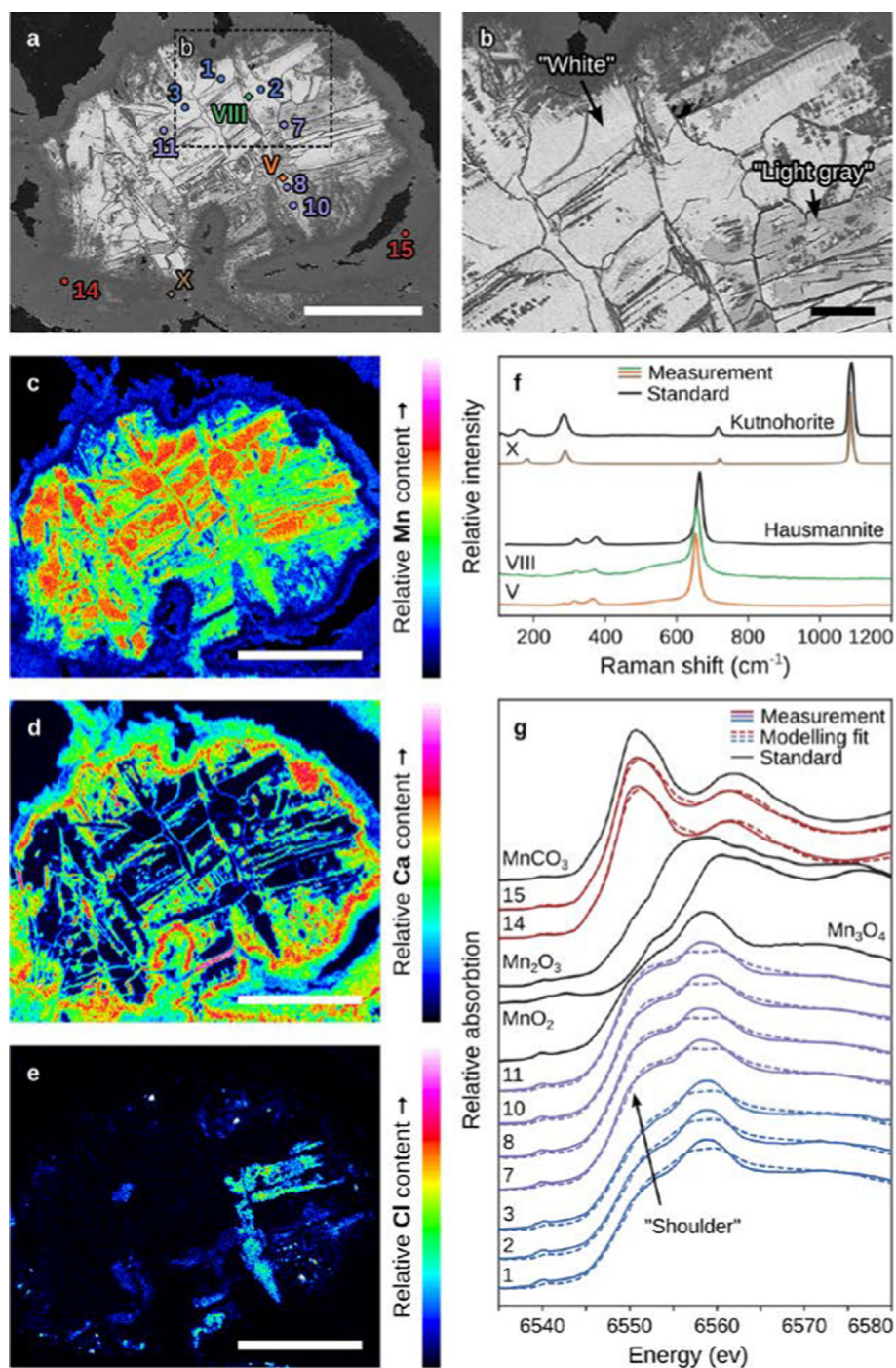


Fig. 5. (a) Back-scattered electron (BSE)-SEM images of Zunyi manganese deposit sample Zunyi-2 showing Mn-oxide phases (white and light grey) as inclusions or unreacted residues in Ca-MnCO₃ nodules (dark grey). (b) Magnified image of the area indicated in panel a, showing cross-cutting Mn carbonate veins in the residual hausmannite core. White and light grey Mn-oxide phases are indicated for clarity. (c-e) Electron probe micro-analysis (EPMA) maps of relative Mn, Ca, and Cl content, respectively, from the Ca-MnCO₃ nodule in panel a. (c) Manganese concentrations differ between “white” and “light grey” Mn-oxide phases. (d) Calcium represents the (Mn-Ca)CO₃ end-member, with Ca concentration mapping showing Mn/Ca-carbonates cross-cutting the Mn-oxides. (e) Chlorine is only present in the “light grey” Mn-oxide phase. (f) Raman spectral comparisons of kutnohorite and hausmannite standards with Mn carbonate (spot X on panel a) “white” (VIII) and “light grey” (V) Mn-oxides, respectively. (g) Manganese K-edge mXANES spectra from Mn standards and spots indicated with same numbers as on panel a. Samples spectra are shown as red (Mn-carbonate matrix), purple (“light grey” Mn-oxides), and blue (“white” Mn-oxides) full lines. Dashed and black lines represent model fits and reference standards, respectively. Reference spectra include MnCO₃, MnO₂, Mn₃O₄, and Mn₂O₃. Scale bars represent 100 μm.

6553 eV (Fig. 5g, S4f) due to the presence of a higher proportion of Mn(II) and less Mn(IV). This is evidenced by the quantitative fit results of the “light grey” Mn-oxides (Table 2 and S3), which show a different proportion of Mn(II), Mn(III), Mn(IV) and average Mn valence state between these two types of Mn oxides (Table 2).

The “dark grey” Mn-carbonate phase is clearly edge-shifted toward much lower E_0 values (6550.7 eV) and the shape of spectrum is similar to that of the Mn(II)CO₃ standard (Fig. 5g, S4f, Table 1). These observations suggest a substantially larger proportion of Mn(II) and a drop in average valence, as reflected in the fit results (Table 2 and S3).

It is important to note that no errors can be given for our Combo method fit results as the method does not suppose that the measured spectra are actually composed of a mixture of the used standards. Instead, the Combo method has been empirically found to give accurate valence estimates if enough different Mn standards are used and if standards with negative loadings are iteratively removed (Manceau et al., 2012). In order to assess the stability of the fit results, we conducted sensitivity tests by adding back deleted standards one by one after that model run. In most cases, re-added standards retained a negative loading; in cases where they had a positive loading, the R-factor was poorer, suggesting that the Combo method produced an optimal fit (see [Supplementary Information](#)).

4.2. Late Devonian Xialei manganese deposit

The minerals present in the Xialei manganese deposit include Mn-carbonates, Mn-Fe silicates, and magnetite (Table S1). EPMA, EDS and laser Raman spectroscopy (Fig. 6c, 7d, S2, S5, Table S1, S2) indicate that the Mn-Fe silicates can be divided into hydrous silicates (e.g., Fe-rich caryopilite [(Mn/Fe)₃(Si₂O₅)(OH)₄] with FeO content up to 13 wt%) and anhydrous silicates (e.g., tephroite and spessartine).

Laminated textures are ubiquitous in the Xialei manganese deposit and characterize the main Mn-carbonate phase (e.g., Fig. 6a, 7a). Back-scattered electron SEM images show that more than half of the Mn-Fe silicates nodules and spherulites are enclosed in Mn-carbonate laminae (Fig. 6a, 7a, 7e, 8a, 8e). The orientation of the nodules and spherulites also defines primary lamination (e.g., Fig. 6a, 8a). These fabrics may be divided into two types.

Type I is represented by samples XL-1 and XL-2 (Figs. 6, 7), in which the nodules and spherulites are mainly Fe-rich caryopilite with some spessartine, tephroite, and magnetite (Fig. 7d). In detail, in sample XL-1, the nodules are spherical to oblate in shape, approximately uniform and typically ~ 500 μm in diameter (e.g., Fig. 6a). The caryopilite aggregates have pelitic, felted, or colloform structures similar to the structure of crystallized gel or glass. Microlaminations in the matrix warp around the caryopilite nodules (Fig. 6b). In EPMA maps, Mn-, Ca-, Fe-, and Si-mapping of a Fe-caryopilite nodule are showed in Fig. 6e-i; in sample XL-2, the spherulites distributed in Mn-carbonate laminae are much smaller and remarkably uniform in size, with a diameter of ~ 10 μm (Fig. 7e, 7f).

Small amounts of tephroite and magnetite also occur at the contact between caryopilite nodules and the Mn-carbonate matrix in sample XL-1 (Fig. 6b, 7b). Tephroite and magnetite replacement of some caryopilite nodules appears to be patchy and incomplete, with relict caryopilite present (Fig. 7b). In other nodules, however, caryopilite has undergone near-complete replacement (Fig. 7c). Tephroite replacement seems to have proceeded from the edges of the caryopilite nodules towards their cores. Nodules comprised of caryopilite have also been overprinted by rounded spessartine crystals, which have destroyed the primary structures; the spessartine grains have been further overprinted by tephroite (Fig. 7b). In addition, some finely dispersed individual tephroite particles are randomly scattered across the laminated Mn-carbonate matrix (Fig. 7a, 7b).

Type II is represented by samples XL-3 and XL-4, in which the main mineral in spherulites is tephroite (Fig. 8, S5) with minor amounts of magnetite (Fig. 8d, 8f). The spherulites show various size among samples but they have uniform size in individual samples, e.g., ~20 μm in diameter in sample XL-3 vs. ~ 400 μm in diameter in sample XL-4. In sample XL-3, magnetite forms thin linings that grade into thicker rims with residual tephroite cores and finally into solid magnetite spheroids (Fig. 8d).

Earlier hypotheses have suggested that Mn(IV) oxyhydroxides were the initially precipitated Mn minerals in sediments. Recent observation of braunite as a prominent Mn(III)-silicate phase in major manganese deposits, interpreted to have formed from a precursor Mn(III)-oxide phase (Urban et al., 1992; Gutzmer and Beukes, 1996; Johnson et al., 2016a), has been brought forward as evidence for the above model. But both the forming process and the precursor phases of braunite remain controversial (Maynard, 2010; Johnson et al., 2016a). The ores studied here are, instead, characterized by large nodules containing Fe-rich caryopilite as the oldest (silicate) mineral phase. In order to determine whether their formation was dependent on an oxidized Mn species, it is necessary to examine whether Mn(III) or Mn(IV) is still present in these caryopilite nodules and to quantify the overall Mn redox state.

Mn and Fe oxidation states in Xialei samples were determined by XPS Mn 3p and Fe 2p analyses. The quantitative curve fit results and curve fits for XPS spectra are illustrated in Fig. 6d and Table S4. The Mn 3p and Fe 2p spectra of all Fe-rich caryopilite samples can be decomposed into different peaks, indicating that Fe and Mn in this mineral have mixed valence, distributed in varying proportions between Fe(II) and Fe(III), and Mn(II), Mn(III), and Mn(IV), respectively. In contrast, the fit results of the Mn 3p spectra from the matrix Mn-carbonate show the presence of Mn(II) only.

5. DISCUSSION

5.1. Mn(III) as an indicator of manganese paragenetic pathways

Marine chemical precipitates are a critical window to view the chemistry and biology of Earth's ancient oceans. With respect to manganese deposits, while the main mineral

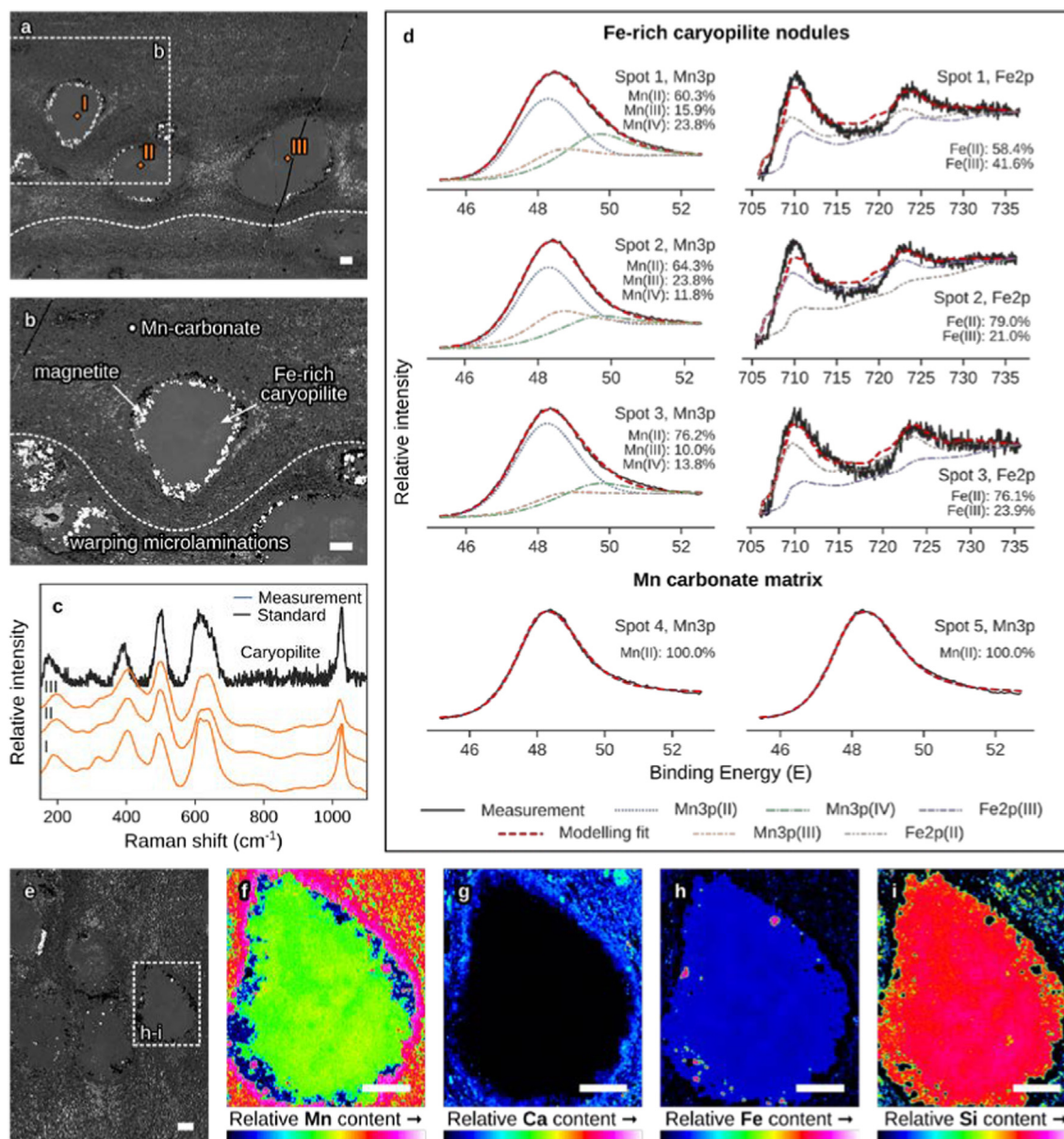


Fig. 6. (a, b) BSE-SEM images of Xialei manganese minerals in sample XL-1 showing nodules comprised mainly of Fe-rich caryopilite in a laminated Mn-carbonate matrix. Undulating dashed line denotes bedding direction. (b) Magnified image of the area indicated on panel (a) shows microlaminations in the matrix warp around the caryopilite nodules (dashed line), indicating that the nodules formed prior to the lithification of the matrix. Magnetite appears along the rims of Fe-rich caryopilite nodules. Scale bars represent 100 μm . (c) Raman spectral comparison of caryopilite standards (black line) with the orange spots indicated in panel (a). (d) X-ray photoelectron spectroscopy (XPS) of Fe-rich caryopilite and Mn-carbonate showing the valence state of Mn and Fe. The Mn 3p and Fe 2p spectra of Fe-caryopilite samples can be decomposed into three peaks, while the Mn 3p spectra of Mn-carbonate only have a single peak. The ratios of different valence for both elements are shown as percentages. (e-i) BSE-SEM image, and EPMA Mn-, Ca-, Fe-, and Si-mapping, respectively, of a Fe-caryopilite nodule. Scale bars represent 100 μm .

phases present today are Mn(II)-carbonates and Mn(II)-silicates (Maynard, 2010; Johnson et al., 2016a), it is widely believed that the primary Mn phases delivered to the seafloor were Mn(IV)-oxides that had precipitated in the oxic layers, rather than Mn(III)-bearing oxides such as manganese or feitknechtite (MnOOH) (Fig. 2a, b; Calvert and Pedersen, 1996; Tebo et al., 2005; Planavsky et al., 2021), as the oxidation of Mn(II) by O_2 via the transfer of a single electron has been demonstrated to be thermodynamically

unfavorable (Bargar et al., 2000, 2005; Luther, 2010). This is supported by the observation that modern-day deep-sea manganese nodules formed on the seafloor are entirely Mn(IV)-oxides and the discovery of microscale Mn(IV) oxide inclusions, interpreted to be residues of primary phase, in early diagenetic carbonate nodules (e.g., Tebo et al., 2004; Johnson et al., 2016a). Upon burial those Mn(IV)-oxides would have been reduced to Mn(II), and then formed diagenetic Mn(II)-carbonates in porewater via the

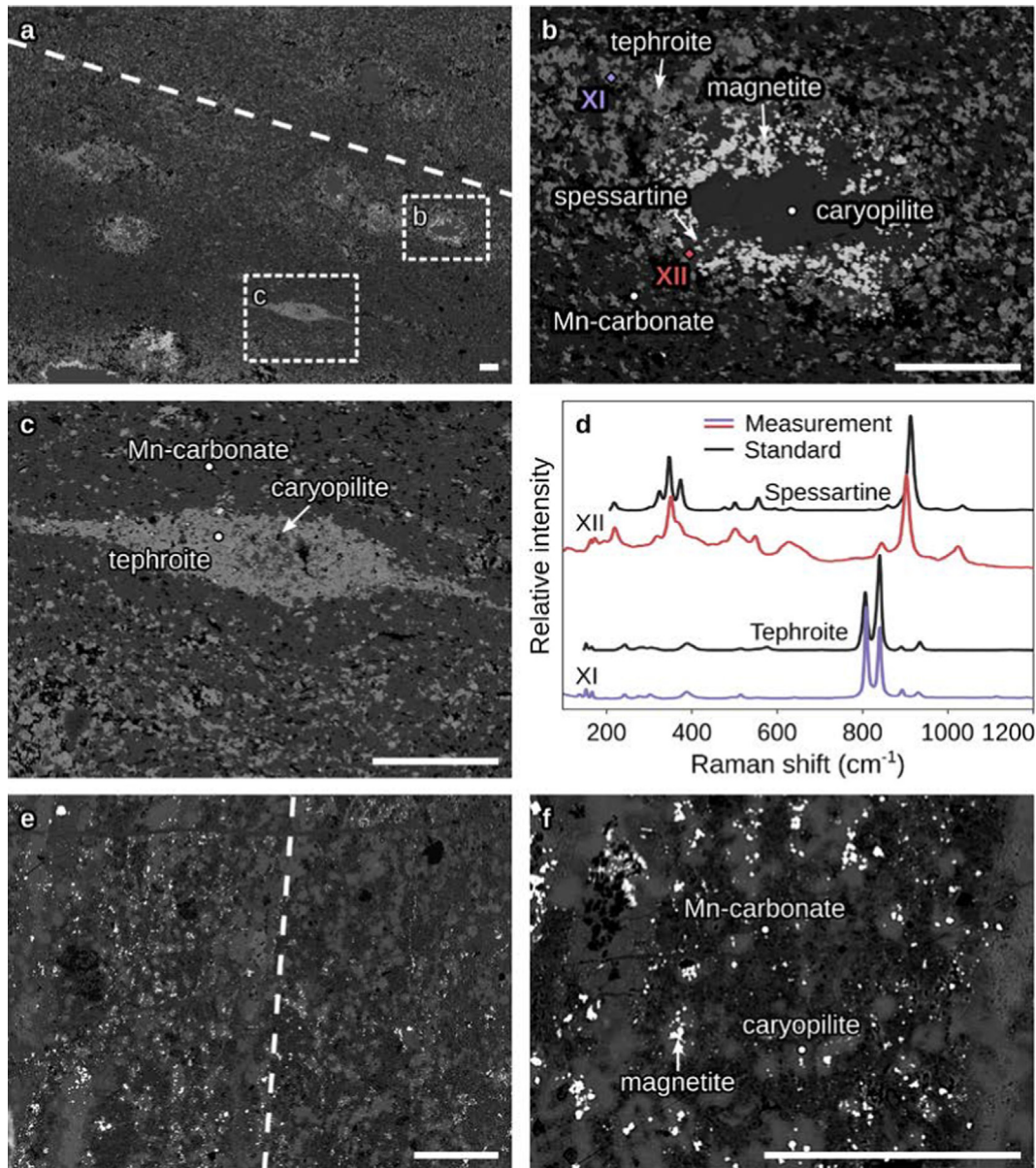
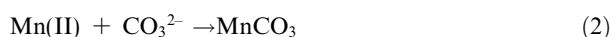
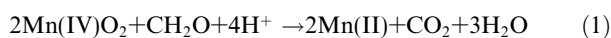


Fig. 7. BSE-SEM images of Xialei manganese minerals displaying Type-I manganese silicate nodules in sample XL-1 (a-d) and Zunyi-2 (e, f). (a) Fe-rich caryopilite nodules in a laminated Mn carbonate matrix (dashed line) displaying varied overprinting. (b-d) Magnified images of caryopilite nodules on panel (a). (b) Nodules of Fe-rich caryopilite are overprinted by round spessartine crystals, which have destroyed primary structures. (c) These spessartine grains are, in turn, overgrown by tephroite and magnetite. (b-c) Starting from the edge of the nodules and moving towards the core, tephroite gradually replaces Fe-rich caryopilite, and finally forms near-complete tephroite nodules. (d) Raman spectra of tephroite (XI) and spessartine (XII) from spots marked on panel (b), compared to mineral reference spectra. (e, f) The Fe-rich caryopilite spherulites with some magnetite particles are finely distributed in laminated Mn carbonate matrix (dashed line). Scale bars represent 100 μm .

following reactions (Okita et al., 1988; Tsikos et al., 2003; Maynard, 2010):



However, this view has recently been challenged. It has been suggested that Mn(II) and CO_3^{2-} concentrations in anoxic seawater were sufficient to allow for the direct nucleation and precipitation of Mn(II)-carbonate (Fig. 2c;

Herndon et al., 2018; Wittkop et al., 2020). This mechanism does not require reductive dissolution of Mn(IV) oxides to form Mn(II)-carbonates, thereby decoupling the presence of reduced Mn-carbonates from the presence of an oxygenated layer in the water column.

Experimental work has further suggested that insoluble Mn(III)-oxide phases, such as feitknechtite, may form during reductive transformation of Mn(IV) to Mn(II) by metal-reducing bacteria and potentially may be important

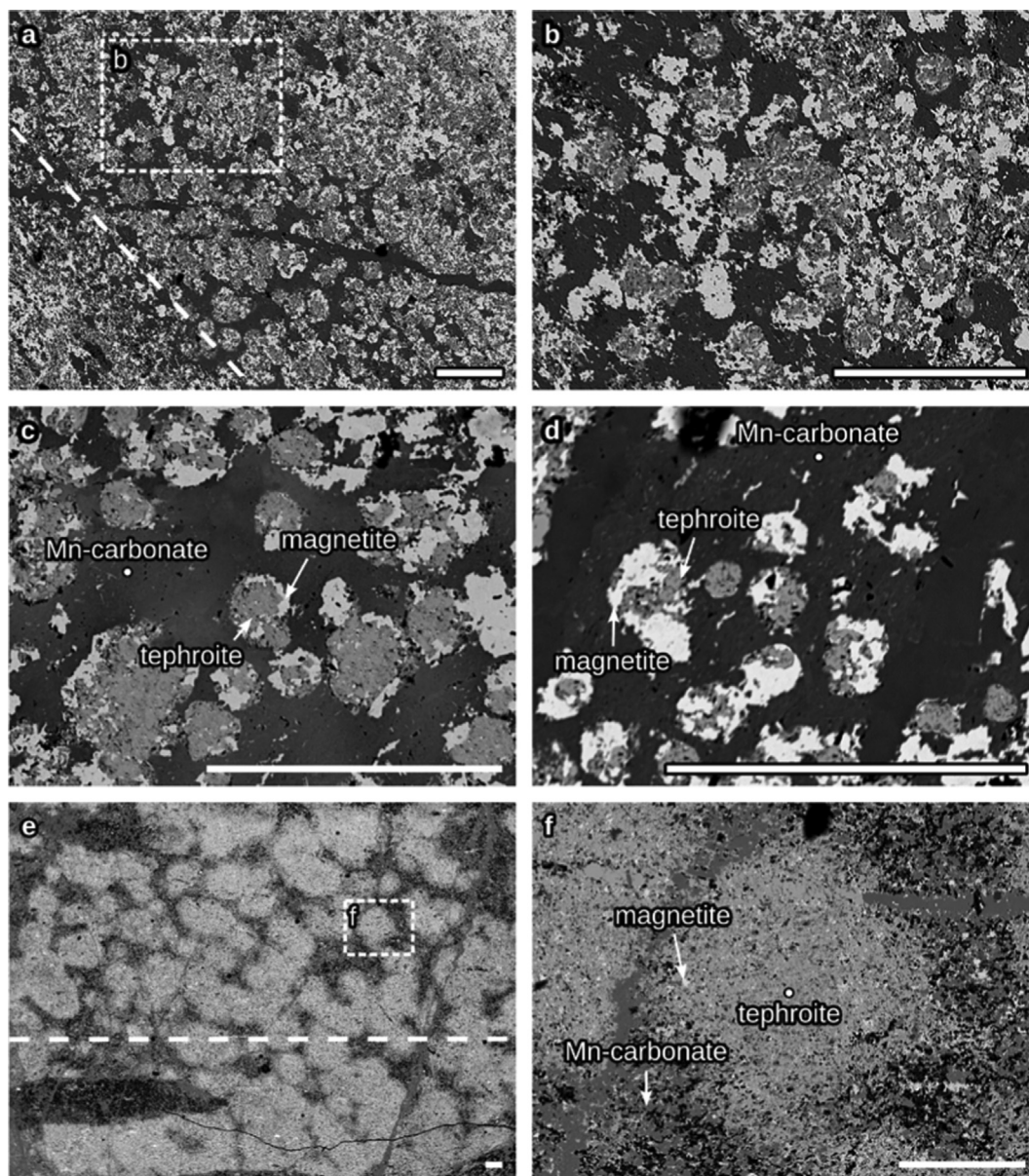
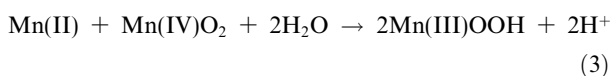


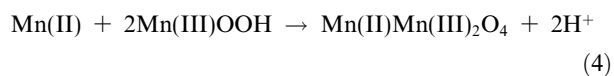
Fig. 8. BSE-SEM images of Type-II manganese silicate nodules in Xialei sample XL-3 (a–d) and XL-4 (e, f). (a–d) Tephroite spherulites are distributed in Mn-carbonate laminae (dashed lines). (c, d) Magnetite forms thin linings that grade into thicker rims with residual tephroite cores and finally into solid magnetite spheroids. (e, f) The spherulites of tephroite are distributed in Mn(II)-carbonate laminae (dashed lines). Magnetite is present as minor components in the spherulites. Scale bars represent 100 μm .

in the redox cycling of Mn (Fig. 2b; e.g., Murray et al. 1985; Parker et al., 2007; Elzinga, 2011; Lin et al., 2012; Madison et al., 2013; Johnson et al., 2016b; Oldham et al., 2017). Specifically, Mn(III)-oxyhydroxides could form when dissolved Mn^{2+} is oxidized during the reduction of remnant Mn(IV) oxides in porewaters:



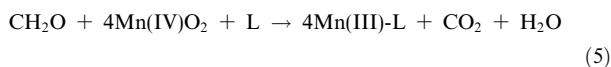
Importantly, this metastable Mn(III) oxyhydroxide (e.g., feitknechtite) is a solid phase that could potentially enter the sedimentary record and subsequently form either

manganite at pH 7.0–7.5 or hausmannite at pH > 8.0 (e.g., Lefkowitz et al., 2013; Elzinga and Kustka, 2015):

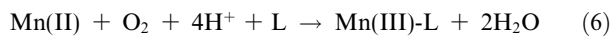


Alternatively, soluble meta-stable organic Mn(III)-ligand complexes (hereafter abbreviated as “L”; e.g., pyrophosphate or siderophores) have also been proposed to be ubiquitous in anoxic systems (Oldham et al., 2015), suboxic waters (Trouwborst et al., 2006; Yakushev et al., 2007, 2009; Dellwig et al., 2012; Madison et al., 2013),

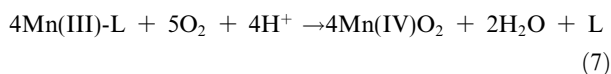
and oxygenated seawater (Oldham et al., 2017). Madison et al. (2013) proposed that soluble Mn(III) could be primarily produced via biotic dissolution of Mn(IV)O₂:



Recent work on the mechanism of bacterial Mn(II) oxidation has demonstrated that Mn(III)-ligand complexes also occur as short-lived intermediates in the oxidation of Mn(II) to Mn(IV) oxides (Webb et al., 2005; Parker et al., 2007; Learman et al., 2011).



However, it is not common to observe substantial accumulations of Mn(III) species because they are subsequently fully oxidized to Mn(IV) oxides.



Therefore, the identification and observation of (meta) stable Mn(III) phases (e.g., hausmannite, feiknechtite or Mn(III)-ligand complexes) in the rock record may help explain the paragenetic sequence of manganese deposits during diagenesis and metamorphism, as these Mn(III) minerals represent important intermediates that primarily capture the reduction of Mn(IV) to Mn(II) or, possibly, Mn(II) oxidation (Tsikos et al., 2003; Johnson et al., 2016b).

5.2. Evidence for early origin of Mn(III)-containing oxides

The petrographic observation of hausmannite in our samples may help constrain the mechanisms outlined above. When compared with the characteristic petrographic structure of Mn(IV)-oxides as inclusions in carbonate nodules, as in Johnson et al. (2016a) and Fang et al. (2020), the hausmannite in our samples is more consistent with an early formed oxidized phase preserved as an unreactive residue, rather than a product of secondary oxidation of Mn(II). The hausmannite in our samples is not likely a weathering product because that process generally produces Mn(IV)-oxide phases (Johnson et al., 2016a). In addition, the “white” hausmannite phases in our samples appear crystalline in fabric, as opposed to a weathering product which generally displays “fluffy” morphology (e.g., Johnson et al., 2016a).

In Ca-rich marine sedimentary environment, Mn-bearing carbonates are generally mixed Mn-Ca carbonates (e.g., kutnohorite) rather than the rhodochrosite endmember (Brand and Veizer, 1980; Neumann et al., 2002; Mucci, 2004), especially since pure rhodochrosite is not a stable phase (Middelburg et al., 1987). The presence of kutnohorite veinlets cross-cutting hausmannite (e.g., Fig. 5d, S4d) indicates that the hausmannite was formed prior to veining. The presence of concentric Mn(II)-carbonate rings surrounding hausmannite nodule cores (Fig. 4c-d) also indicates that the rings were formed on a reacted residual core of hausmannite. By contrast, petrographic observations representing a direct Mn(II)-carbonate precipitation pathway where some fine-grained calcite crystals are surrounded

by Mn(II)-carbonates as observed in other Mn(II)-carbonate deposits (Gao et al., 2021; Chen et al., 2022) are lacking in our samples. Overall, the petrographic features in our samples suggest that Mn(II)-carbonates were derived from Mn-oxides, and most likely in association with secondary reduction coupled to organic carbon oxidation. This finding is consistent with the isotope compositions of Mn(II)-carbonates (e.g., Okita et al., 1988; Okita, 1992; Maynard, 2010).

As described above, the “white” Mn-oxide minerals have a solid mineralized texture, while the “light grey” minerals appear fuzzy and contain Cl (Fig. 5b, 5e, S3a, S3d, S4a, S4e). It is likely that the “light grey” hausmannite is a poorly crystallized analogue for the “white” phase, but the textural relationships are unclear as to whether these phases precipitated at the same time, or if one derived from the other. However, based on the μ XANES spectra and the fitting results, the valence of the “light grey” phase is lower than that of the “white” hausmannite but higher than that of Mn(II)-carbonate phase (Table 2 and S3), which implies that the “light grey” hausmannite may be the intermediate product recording the transition from the oxidized “white” phase to reduced Mn(II)-carbonates.

The origin of the high Cl content is unclear but could be attributed to the incorporation of Cl into chemical sediments either in the water column or within the sediment pile. To the best of our knowledge a Cl-containing Mn-oxide has not been previously suggested or shown to form under the seawater-like conditions relevant to our discussion. Yet, in light of the similarities between Mn and Fe, and the identification of an Fe(II,III) green rust phase ([Fe(II)₃Fe(III)(OH)⁸⁺•Cl⁻•nH₂O]; Zegeye et al., 2012; Halevy et al., 2017), which may be reduced to Fe(II)-carbonate during diagenesis, we suggest that a mixed valence Mn-oxyhydroxide-chloride phase could be formed in a similar manner. Overall, since Mn(IV)O₂ is not observed in our samples, a reductive process from Mn(IV)O₂ to Mn(III)-oxide and further to Mn(II)-carbonate seems reasonable.

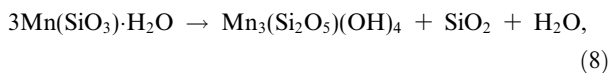
5.3. Evidence for oxidative origin of Mn-silicates

Petrographic signatures of the Mn(II)-silicate nodules and spherulites in the Xialei samples have strong implications for the mechanisms of their formation. The textures defining the sedimentary lamination are enclosed in diagenetic Mn(II)-carbonate laminations (e.g., Fig. 6a), which precludes a late-stage diagenetic or metamorphic origin. Warping microlaminations around caryopillite nodules (Fig. 6b) further indicate that lithification of the nodules must have occurred during early diagenesis before matrix compaction while the sediments still had high porosity and water content. The low Al and K contents (Fig. S2, Table S1) and remarkably uniform sizes and shapes within a given sample also exclude the possibility of a detrital origin. Instead, the nodule and spherulite textures are best interpreted as primary authigenic sedimentary textures formed during deposition and/or the earliest phase of diagenesis. Similar textures have been described in BIF in which microgranules of Fe-silicate define primary

lamination and are enclosed by early diagenetic chert mesobands (Krapež et al., 2003; Rasmussen et al., 2013, 2015, 2017) and in Ediacaran chert nodules around which micro-laminations in the matrix warp (Xiao et al., 2010). In addition, Mn(II)-silicate minerals characterized by μm -sized glassy textures and nodule structures have also been reported in the Mn-rich sediments in the Ural Mountains in Russia and considered to represent primary sedimentary features (Flohr and Huebner, 1992; Brusnitsyn, 2006; Brusnitsyn et al., 2017).

Among the present Mn(II)-silicate phases in the Xialei manganese deposit, textural relationships indicate that Fe-rich caryopilite was formed the earliest. Caryopilite is a characteristic mineral of low-grade regional metamorphism and is most common in Mn-rich metasediments. Previous studies proposed that caryopilite derived from the alteration and silicification of Mn(II)-carbonate during late diagenesis or metamorphism (Fig. 2a; Maynard, 2010; Johnson et al., 2016a). However, in our samples, this explanation is challenged by the presence of early-formed caryopilite nodules and spherulites and the absence of late-stage Si veins. In addition, in Xialei samples where silica-rich fluids have moved through discrete veins or faults and reacted with Mn(II)-carbonate, the formation product is rhodonite (a high-temperature metamorphic Mn(II)-silicate), not caryopilite (Zeng and Liu, 1999; Chen et al., 2018).

Alternatively, Manceau and Gallup (2005) have shown that at a geothermal field in Indonesia, a poorly crystalline Mn(II)-rich hydrous silicate, with a glassy texture, precipitates from a hydrothermal brine. In this geothermal system, Mn directly precipitates with silica under anoxic conditions. Experiments have also shown that in O_2 -free and alkaline (pH 10) solutions, nanometer-sized Mn(II)-rich phyllosilicates can be synthesized by mixing Mn(II) and silica at 150°C (Manceau and Gallup, 2005). Particularly, the cloudy, globular, and cryptocrystalline textures of the caryopilite aggregates from our samples are similar to gel or glass textures. In an anoxic ocean, dissolved Mn(II) could have combined directly with silica in the water column, forming the precursor to caryopilite, possibly a Mn-rich, Mg/Al-poor silicate precursor such as gonyerite ($[(\text{Mn}^{2+}, \text{Mg})_5\text{Fe}^{3+}(\text{Fe}^{3+}\text{Si}_3\text{O}_{10})(\text{OH})_8]$, a marine Mn mineral from the chlorite group) or neotocite ($[(\text{MnSiO}\cdot n\text{H}_2\text{O})]$, an unmetamorphosed, diagenetic mineral) (Flohr and Huebner, 1992; Brusnitsyn, 2006; Brusnitsyn et al., 2017). This precursor could then have undergone alteration in the sediment pile, releasing silica:



A similar caryopilite genesis pathway has been previously suggested by researchers studying the manganese deposits of the Urals (Brusnitsyn et al., 2017).

Some lines of evidence, however, apparently contradict an anoxic origin for caryopilite. For example, XPS valence quantification shows that the caryopilite contains detectable Mn(III,IV) (Fig. 6d). As greenalite – the Fe-equivalent mineral for caryopilite – is known to host variable compositions of mixed-valence Fe(II,III) (Johnson

et al., 2018), we suggest that our Raman and XPS data can be simply reconciled by a caryopilite phase that similarly hosts variable amounts of Mn(III,IV) in addition to Mn(II). This demands an oxidative mechanism, which argues against purely anoxic conditions where Mn(II)-Si gels can be formed. Although the possibility that Mn(III, IV) and Fe(III) were secondarily acquired cannot be explicitly ruled out, the absence of a spatially coherent redox distribution suggests that Mn(III,IV) and Fe(III) were original components of the caryopilite rather than the products of a secondary fluid front. In addition, secondary oxidizing fluids moving through discrete veins or faults generally transform Mn(II) phases to Mn(IV) oxides, rather than Mn(III) phases (Johnson et al., 2016a).

A model for the formation of Mn(II,III,IV)-caryopilite that is consistent with the findings of this study invokes dissolved metastable Mn(III)-ligand complexes (Madison et al., 2013) produced via oxidation of Mn(II) in aqueous environments as the initial precursor phases. Dissolved oxygen and silica present in the oceans could have induced the transformation of Mn(III)-ligand complexes into thermodynamically more favorable Mn(III,IV)-bearing Mn-Si phases during particle descent. Early diagenesis could have involved some Mn-reducing microbes which utilized the oxidized manganese and promoted the transformation of Mn(III,IV)-bearing Mn-Si phases into Mn(II,III,IV)-caryopilite. This model is similar to the mechanism for the formation of Fe(III)-bearing greenalite from the combination of an initial Fe(II,III) precursor metastable phase (green rust) with dissolved silica (Johnson et al., 2018).

An alternative, and perhaps more plausible, pathway for the formation of Mn(II,III,IV)-caryopilite through Mn(IV)-oxides is hypothesized. Hausmannite has been proposed in the Zunyi samples as a product of the reductive transformation of Mn(IV)-oxides to Mn(II) (see Section 5.2). The presence of hausmannite in the cores of Mn(II)-carbonate nodules implies that the Mn(III,IV)-silicate precursor of the caryopilite could also have derived from the reduction of an initial Mn(IV)-oxide, which is the final product of the full oxidation of Mn(II). In previous studies, to keep Mn(IV) from becoming fully reduced to Mn(II), (meta)stable Mn(III)-L complexes (Madison et al., 2013) or the formation of Mn(III)-oxyhydroxides (Murray et al., 1985; Johnson et al., 2016b) were invoked. These Mn(III,IV) phases could have interacted with aqueous H_4SiO_4 and then been transformed into more stable Mn(III,IV)-containing caryopilite during early diagenesis in the sediments, similar to the formation mechanism proposed for braunite (Johnson et al., 2016a; Johnson, 2019).

Thus, both the transformation of primary Mn(III)-ligands and the reduction of an initial Mn(IV)-oxide in a silica-rich (micro)environment remain plausible pathways to the formation of a Mn(II,III,IV)-silicate precursor to caryopilite. Fully evaluating these two hypotheses requires additional experimental work, yet our characterization of Mn(II,III,IV)-caryopilite as the earliest-formed Mn-silicate phase in our samples, combined with previous reports of mixed-valence braunite (Johnson et al., 2016a), point towards the Mn(IV)-oxide pathway. The nodule and spherulite textures could be have formed when

continued reduction of precursor phases during subsequent diagenesis and metamorphism (Fig. 9). Alternatively, the oxidation of Mn(II) in silica-enriched water could also have directly led to the precipitation of Mn(III,IV)-bearing silicates, which were precursors to a variety of Mn(II)-silicates (Fig. 9). In either event, the identification of Mn(III) mineral phases, formed through Mn(II) oxidation or Mn(IV) reduction, in other Mn ore deposits would provide additional support for the paragenetic model presented here and the role that the water column oxidation of Mn(II) as an important process in the formation of Mn ores.

The paragenetic model described here, based on new observations of the Zunyi and Xiaiei Mn deposits, is reminiscent of the previously suggested oxidative formation pathway of Mn(II)-carbonate (Maynard, 2010; Johnson et al., 2016a). However, the paragenetic model is advanced with the discovery of Mn(II,III)-bearing oxides (e.g., hausmannite), which are important intermediates from the reduction of Mn(IV)-oxides. The fact that Mn(II,III)-oxide residues were found only in the samples with the highest Mn contents implies that the preservation of original manganese oxides may depend on a balance between the amounts of organic carbon or other reductants and the oxidized Mn (Konhauser, 2007). In organic-rich marine sedimentary basins, preservation of these residues may be difficult. A consequence of this is that the intermediate Mn(II,III)-oxide phases may not be preserved in other Mn deposits formed where there is a greater flux of organic carbon to the sediment pile, obscuring the full expression of this paragenetic model.

A significant difference between our model and prior models based on data from other Mn deposits is the formation stage of the Mn-silicate phases. While previous models considered that Mn-silicates precipitated later than Mn-carbonates and were the product of reactions with SiO₂ during metamorphism (e.g., Maynard, 2010), the Mn(III,IV)-silicate precursor phases in this study were identified to be formed during early diagenesis, or perhaps even earlier. This is evidenced by the observation that Mn(II)-silicate nodules/spherulites are embedded in the Mn(II)-carbonate matrix, instead of cross-cutting it. In accordance with the model proposed earlier for braunite (Johnson et al., 2016a), these silicates were likely formed via the combination Mn(III)-oxides or Mn(III)-L complexes with silica during the diagenetic reduction of Mn(IV) oxides. Many other Mn silicates (caryopilite, tephroite, pyroxmangite) were subsequently formed in consecutive transformations of these Mn silicate precursor phases.

Our model for Mn paragenesis indicates that the formation of the Zunyi and Xiaiei deposits and, perhaps, other ancient marine Mn deposits required seawater or porewater enriched in silica. It has been commonly proposed that the main source of manganese for ancient Mn deposits was hydrothermal venting from deep-water volcanic ridge systems (e.g., Maynard, 2010). Our model favors this viewpoint, as hydrothermal introduction of both manganese and silica to seawater can explain the presence of sufficient quantities of both reactants, possibly more easily than post-depositional addition of silica-enriched hydrothermal fluids during metamorphism in the alternative mechanism.

It is difficult to envision the correct amount of silica being introduced post-depositionally to produce Mn(II)-silicates throughout the entire formation. Detailed petrographical and in-situ chemical studies of other ancient Mn deposits are required to determine the presence of Mn(III)-oxides and/or silicates and to assess the wider applicability of the proposed Mn paragenesis pathway for other Mn ore deposits. This is especially true for those deposits formed in the Paleoproterozoic and for which cryptic signals for ancient oxygen may be present.

6. CONCLUSIONS

A combination of scanning electron microscopy, laser Raman spectroscopy analysis, X-ray photoelectron spectroscopy, and X-ray absorption spectroscopy were used to examine Mn-oxide, -carbonate, and -silicate minerals from the late Devonian Xiaiei and middle-late Permian Zunyi manganese deposits from South China. This allowed for a petrogenetic model to be developed in a framework that informs our understanding of ancient Mn cycling. Although recent studies have proposed that Mn(II)-carbonate and -silicate minerals, common in ancient manganese deposits, could be formed by direct precipitation in anoxic waters, the discovery of “residual” Mn(II,III) oxide mineral (hausmannite) in Mn(II)-carbonate nodules directly challenges this in the case of our samples. In addition, the best-preserved Fe-rich caryopilite nodules and spherulites host variable levels of Mn(III,IV) and Fe(III), indicating that an oxidative mechanism was required during sedimentation. Therefore, our results support the utility of Mn phases as proxies for water columns that were characterized by a sufficient oxidizing potential to result in Mn(II) oxidation. Additionally, the findings presented here highlight the significant role that Mn(III) phases may have played in the biogeochemical redox cycling of Mn in Earth’s ancient oceans.

RESEARCH DATA

Research data are presented as an Electronic Annex [Supplementary Materials](#) Tables and Figures.

Declaration of Competing Interest

The authors declare that they have no known competing financial interests or personal relationships that could have appeared to influence the work reported in this paper.

ACKNOWLEDGMENTS

Funding for this research was provided by the National Natural Science Foundation of China (41972091), the consulting research project of the Chinese Academy of Engineering (no. 2021-XBZD-6-4) and the special fund from the State Key Laboratory of Geological Processes and Mineral Resources, China University of Geosciences (no. MSFGPMR03-2). We are grateful to Dr. Kui-Dong Zhao, Shui-Yuan Yang and Wei Chen for assistance with lab work, and Executive Editor Jeffrey Catalano, Associate Editor Caroline Peacock and three anonymous reviewers for improving the interpretations of the manuscript.

APPENDIX A. SUPPLEMENTARY DATA

Supplementary data to this article can be found online at <https://doi.org/10.1016/j.gca.2022.03.030>.

REFERENCES

- Alcott L. J., Mills B. J. W. and Poulton S. W. (2019) Stepwise Earth oxygenation is an inherent property of global biogeochemical cycling. *Science* **366**, 1333–1337.
- Anbar A. D. and Holland H. D. (1992) The photochemistry of manganese and the origin of banded iron formations. *Geochim. Cosmochim. Acta* **56**, 2595–2603.
- Armstrong F. A. (2008) Why did nature choose manganese to make oxygen? *Philos. Trans. R. Soc. B Biol. Sci.* **363**, 1263–1270.
- Bagherpour B., Bucher H., Yuan D. X., Leu M., Zhang C. and Shen S. Z. (2018) Early Wuchiapingian (Lopingian, Late Permian) drowning event in the South China Block related to a late eruptive phase of Emeishan Large Igneous Province? *Global Planet Change* **169**, 119–132.
- Bargar J. R., Tebo B. M. and Villinski J. E. (2000) In situ characterization of Mn(II) oxidation by spores of the marine *Bacillus* sp strain SG-1. *Geochim. Cosmochim. Acta* **64**, 2775–2778.
- Bargar J. R., Tebo B. M., Bergmann U., Webb S. M., Glatzel P., Chiu V. Q. and Villalobos M. (2005) Biotic and abiotic products of Mn(II) oxidation by spores of the marine *Bacillus* sp. strain SG-1. *Am. Mineral.* **90**, 143–154.
- Bekker A., Slack J., Planavsky N., Krapež B., Hofmann A., Konhauser K. O. and Rouxel O. J. (2010) Iron formation: the sedimentary product of a complex interplay among mantle, tectonic, oceanic, and biospheric processes. *Econ. Geol.* **105**, 467–508.
- Bekker A., Planavsky N. J., Krapež B., Rasmussen B., Hofmann A., Slack J. F., Rouxel O. J. and Konhauser K. O. (2014) Iron formations: their origins and implications for ancient seawater chemistry. In *Treatise of Geochemistry* (eds. H. D. Holland and K. K. Turekian). Elsevier, pp. 561–628.
- Brand U. and Veizer J. (1980) Chemical diagenesis of a multicomponent carbonate system; 1, Trace elements. *J. Sediment. Res.* **50**, 1219–1236.
- Brunsnitsyn A. I. (2006) Mineralogy and metamorphism conditions of manganese ore at the South Faizulino deposit, the southern Urals, Russia. *Geol. Ore Deposits* **48**, 193–214.
- Brunsnitsyn A. I., Starikova E. V. and Zhukovd I. G. (2017) Mineralogy of low grade metamorphosed manganese sediments of the Urals: Petrological and geological applications. *Ore Geol. Rev.* **85**, 140–152.
- Biesinger M. C., Payne B. P., Grosvenor A. P., Lau L. W. M., Gerson A. R. and Smart R. St C. (2011) Resolving surface chemical states in XPS analysis of first row transition metals, oxides and hydroxides: Cr, Mn, Fe, Co and Ni. *Appl. Surf. Sci.* **257**, 2717–2730.
- Calvert S. E. and Pedersen T. F. (1996) Sedimentary geochemistry of manganese: implications for the environment of formation of manganiferous black shales. *Econ. Geol.* **91**, 36–47.
- Chen W. Y., Liu J. R., Wang Z. G. and Zheng Q. L. (2003) During the Permian emeishan basalt explosion in Guizhou Province. *Journal of Palaeogeography* **5**, 17–28 (in Chinese with English abstract).
- Chen C. L. and Shi X. Y. (2006) Sedimentary and tectonic evolution of Late Paleozoic deep-water strata in the Youjiang basin. *Geol. China* **33**, 436–443, [in Chinese with English abstract].
- Chen D. Z., Wang J. G., Racki G., Li H., Wang C. Y., Ma X. P. and Whalen M. T. (2013) Large sulfur isotopic perturbations and oceanic changes during the Frasnian-Famennian transition of the Late Devonian. *J. Geol. Soc. London* **170**, 465–476.
- Chen F. G., Wang Q. F., Yang S. J., Zhang Q. Z., Liu X. F., Chen J. H. and Carranza E. J. M. (2018) Space time distribution of manganese ore deposits along the southern margin of the South China Block, in the context of Palaeo-Tethyan evolution. *Int. Geol. Rev.* **60**, 72–86.
- Chen F. G., Pufahl P. K., Wang Q. F., Matheson E. J., Shabaga B. M., Zhang Q. Z., Zeng Y. S., Le X. W., Ruan D. and Zhao Y. T. (2022) A New Model for the Genesis of Carboniferous Mn Ores, Longtou deposit, South China Block. *Econ. Geol.* **117**, 107–125.
- Cerrato J. M., Hochella M. F., Knocke W. R., Dietrich A. M. and Cromer T. F. (2010) Use of XPS to identify the Oxidation State of Mn in Solid Surfaces of Filtration Media Oxide Samples from Drinking Water Treatment Plants. *Environ. Sci. Technol.* **44**, 5881–5886.
- Cerrato J. M., Knocke W. R., Hochella M. F., Dietrich A. M., Jones A. and Cromer T. F. (2011) Application of XPS and Solution Chemistry Analyses to Investigate Soluble Manganese Removal by MnOx(s)-Coated Media. *Environ. Sci. Technol.* **45**, 10068–10074.
- Daye M. K., Lepac-Ceraj V., Pajusalu M., Rowland S., Farrell-Sherman A., Beukes N., Tamura N., Fournier G. and Bosak T. (2019) Light-driven anaerobic microbial oxidation of manganese. In *Nature*, 576, pp. 311–314. *Nature*.
- Dellwig O., Schnetger B., Brumsack H. J., Grossart H. P. and Umlauf L. (2012) Dissolved reactive manganese at pelagic redoxclines (part II): hydrodynamic conditions for accumulation. *J. Mar. Syst.* **90**, 31–41.
- Deng J. and Wang Q. F. (2016) Gold mineralization in China: Metallogenic provinces, deposit types and tectonic framework. *Gondwana Res.* **36**, 219–274.
- Dick G. J., Clement B. G., Webb S. M., Fodrie F. J., Bargar J. R. and Tebo B. M. (2009) Enzymatic microbial Mn(II) oxidation and Mn biooxide production in the Guaymas Basin deep-sea hydrothermal plume. *Geochim. Cosmochim. Acta* **73**, 6517–6530.
- Du Y. S., Huang H., Yang J. H., Huang H. W., Tao P., Huang Z. Q., Hu L. S. and Xie C. X. (2013) The basin translation from late Paleozoic to Triassic of the Youjiang basin and its tectonic significance. *Geol. Rev.* **59**, 1–10, [in Chinese with English abstract].
- Elzinga E. J. (2011) Reductive transformation of birnessite by aqueous Mn(II). *Environ. Sci. Technol.* **45**, 6366–6372.
- Elzinga E. J. and Kustka A. B. (2015) A Mn-54 radiotracer study of Mn isotope solid-liquid exchange during reductive transformation of vernadite (δ -MnO₂) by aqueous Mn (II). *Environ. Sci. Technol.* **49**, 4310–4316.
- El Rhazi M. and Hayashi K. I. (2003) Origin and formational environment of Noda-Tamagawa manganese ore, northeast Japan: constraints from isotopic studies. *Chem. Erde* **63**, 149–162.
- Fang H., Tang D. J., Shi X. Y., Lechte M., Shang M. H., Zhou X. Q. and Yu W. C. (2020) Manganese-rich deposits in the Mesoproterozoic Gaoyuzhuang Formation (ca. 1.58 Ga), North China Platform: Genesis and paleoenvironmental implications. *Palaeogeogr. Palaeoclimatol. Palaeoecol.* **559** 109966.
- Farges F. (2005) Ab initio and experimental pre-edge investigations of the Mn K-edge XANES in oxide-type materials. *Phys. Rev. B* **71** 155109.
- Farquhar J., Zerkle A. L. and Bekker A. (2014) Geologic and geochemical constraints on Earth's early atmosphere. *Treat. Geochem.* **6**, 91–138.

- Flohr M. J. K. and Huebner J. S. (1992) Mineralogy and geochemistry of two metamorphosed sedimentary manganese deposits, Sierra-Nevada, California, USA. *Lithos* **29**, 57–85.
- Gao J. B., Yang R. D., Xu H., Zhang X., Feng K. N. and Zheng L. L. (2018) Genesis of Permian sedimentary manganese deposits in Zunyi, Guizhou Province, SW China: Constraints from geology and elemental geochemistry. *J. Geochem. Explor.* **192**, 142–154.
- Gao Z. F., Zhu X. K., Wang D., Pan C. X., Yan B. and Li J. (2021) Insights into hydrothermal controls and processes leading to the formation of the Late Ediacaran Gaoyan stratiform manganese-carbonate deposit, Southwest China. *Ore Geol. Rev.* **139** 104524.
- Gunter T. E., Gavin C. E., Aschner M. and Gunter K. K. (2006) Speciation of manganese in cells and mitochondria: A search for the proximal cause of manganese neurotoxicity. *Neurotoxicol.* **27**, 765–776.
- Gutzmer J. and Beukes N. J. (1996) Mineral paragenesis of the Kalahari manganese field, South Africa. *Ore Geol. Rev.* **11**, 405–428.
- Halevy I., Alesker M., Schuster E. M., Popovitz-Biro R. and Feldman Y. (2017) A key role for green rust in the Precambrian oceans and the genesis of iron formations. *Nat. Geosci.* **10**, 135–139.
- Hansel C. M., Zeiner C. A., Santelli C. M. and Webb S. M. (2012) Mn(II) oxidation by an ascomycete fungus is linked to superoxide production during asexual reproduction. *Proc. Natl. Acad. Sci.* **109**, 12621–12625.
- Heath G. R. and Dymond J. (1977) Genesis and transformation of metalliferous sediments from the East Pacific Rise, Bauer Deep, and Central Basin, northwest Nazca plate. *Geol. Soc. Am. Bull.* **88**, 723–733.
- Herndon E. M., Havig J. R., Singer D. M., McCormick M. L. and Kump L. R. (2018) Manganese and iron geochemistry in sediments underlying the redox-stratified Fayetteville Green Lake. *Geochim. Cosmochim. Acta* **231**, 50–63.
- Ilton E. S., Post J. E., Heaney P. J., Ling F. T. and Kerisit S. N. (2016) XPS determination of Mn oxidation states in Mn (hydr) oxides. *Appl. Surf. Sci.* **366**, 475–485.
- Johnson J. E., Webb S. M., Thomas K., Ono S., Kirschvink J. L. and Fischer W. W. (2013) Manganese-oxidizing photosynthesis before the rise of cyanobacteria. *Proc. Natl. Acad. Sci.* **110**, 11238–11243.
- Johnson J. E., Webb S. M., Ma C. and Fischer W. W. (2016a) Manganese mineralogy and diagenesis in the sedimentary rock record. *Geochim. Cosmochim. Acta* **173**, 210–231.
- Johnson J. E., Savalia P., Davis R., Kocar B. D., Webb S. M., Neilson K. H. and Fischer W. W. (2016b) Real-time manganese phase dynamics during biological and abiotic manganese oxide reduction. *Environ. Sci. Technol.* **50**, 4248–4258.
- Johnson J. E., Muhling J. R., Cosmidis J., Rasmussen B. and Templeton A. S. (2018) Low-Fe(III) greenalite was a primary mineral from neoproterozoic oceans. *Geophys. Res. Lett.* **45**, 3182–3192.
- Johnson J. E. (2019) From minerals to metabolisms: Evidence for life before oxygen from the geological record. *Adv. Free Radical Biol. Med.* **140**, 126–137.
- Jun Y. S. and Martin S. T. (2003) Microscopic Observations of Reductive Manganite Dissolution under Oxidic Conditions. *Environ. Sci. Technol.* **37**, 2363–2370.
- Junta J. and Hochella M. F. (1994) Manganese (II) oxidation at mineral surfaces. A microscopic and spectroscopic study. *Geochim. Cosmochim. Acta* **58**, 4985–4999.
- Kelly S. D., Hesterberg D. and Ravel B. (2008) Analysis of soils and minerals using X-ray absorption spectroscopy. In *Methods of soil analysis* (eds. A. L. Ulery and L. R. Drees). Soil Science Society of America, Madison, Wisconsin, USA, pp. 387–463.
- Konhauser K. O., Newman D. K. and Kappler A. (2005) The potential significance of microbial Fe(III)-reduction during Precambrian banded iron formations. *Geobiology* **3**, 167–177.
- Konhauser K. O. (2007) *Introduction to Geomicrobiology*. Blackwell, Oxford, pp. 1–425.
- Konhauser K. O., Planavsky N. J., Hardisty D. S., Robbins L. J., Warchola T. J., Hugaard R., Lalonde S. V., Partin C. A., Oonk P. B. H., Tsikos H., Lyons T. W., Bekker A. and Johnson C. M. (2017) Iron formations: a global record of Neoproterozoic to Palaeoproterozoic environmental history. *Earth Sci. Rev.* **172**, 140–177.
- Krapež B., Barley M. E. and Pickard A. L. (2003) Hydrothermal and resedimented origins of the precursor sediments to banded iron formations: sedimentological evidence from the early Palaeoproterozoic Brockman Supersquence of Western Australia. *Sedimentology* **50**, 979–1011.
- Learman D. R., Voelker B. M., Vazquez-Rodriguez A. I. and Hansel C. M. (2011) Formation of manganese oxides by bacterially generated superoxide. *Nat. Geosci.* **4**, 95–98.
- Lefkowitz J. P., Rouff A. A. and Elzinga E. J. (2013) Influence of pH on the reductive transformation of birnessite by aqueous Mn(II). *Environ. Sci. Technol.* **47**, 10364–10371.
- Lenz C., Behrends T., Jilbert T., Silveira M. and Slomp C. P. (2014) Redox-dependent changes in manganese speciation in Baltic Sea sediments from the Holocene Thermal Maximum: an EXAFS, XANES and LA-ICP-MS study. *Chem. Geol.* **370**, 49–57.
- Li W. J., Peng Z. D., Dong Z. G., Zhang B. L., Gao B. Y., Zhang L., Zhu M. T., Robbins L. J. and Konhauser K. O. (2022) Direct Re-Os dating of manganese carbonate ores and implications for the formation of the Ortokarnash manganese deposit, Northwest China. *Econ. Geol.* **117**, 237–252.
- Lin H., Szeinbaum N. H., Dichristina T. J. and Taillefert M. (2012) Microbial Mn(IV) reduction requires an initial one-electron reductive solubilization step. *Geochim. Cosmochim. Acta* **99**, 179–192.
- Lingappaa U. F., Monteverdea D. R., Magyara J. S., Valentinea J. S. and Fischera W. W. (2019) How manganese empowered life with dioxygen (and vice versa). *Free Radical Biol. Med.* **140**, 113–125.
- Liu W. N., Hao J. H., Elzinga E. J., Piotrowiak P., Nanda V., Yee N. and Falkowski P. G. (2020) Anoxic photogeochemical oxidation of manganese carbonate yields manganese oxide. *Proc. Natl. Acad. Sci.* **117**, 22698–22704.
- Liu Z. C., Zhou Q., Yan J. X., Wang Y., Chen D., Zhou Y. L. and Qin X. J. (2019) Structure of Zunyi rift basin in Guizhou Province during the Permian and its controlling on manganese deposits. *J. Palaeogeogr.* **21**, 517–526, in Chinese with English abstract.
- Luther G. W. (2010) The role of one- and two-electron transfer reactions in forming thermodynamically unstable intermediates as barriers in multi-electron redox reactions. *Aquat. Geochem.* **16**, 395–420.
- Lyons T. W., Reinhard C. T. and Planavsky N. J. (2014) The rise of oxygen in Earth's early ocean and atmosphere. *Nature* **506**, 307–315.
- Ma X. P., Gong Y. M., Chen D. Z., Racki G., Chen X. Q. and Liao W. H. (2016) The Late Devonian Frasnian-Famennian Event in South China — Patterns and causes of extinctions, sea level changes, and isotope variations. *Palaeogeogr. Palaeoclimatol. Palaeoecol.* **448**, 224–244.
- Ma Y. S., Chen H. D., Wang G. L., Guo T. L., Tian J. C., Liu W. J., Xu X. S., Zheng R. C., Mou C. L. and Hou M. C. (2009) *Sequence stratigraphy and Paleogeography in south China: Beijing*. China Science Publishing, pp. 289–291, [in Chinese with English abstract].

- Madison A. S., Tebo B. M., Mucci A., Sundby B. and Luther G. W. (2013) Abundant Mn(III) in porewaters is a major component of the sedimentary redox system. *Science* **341**, 875–878.
- Manceau A., Gorshkov A. I. and Drits V. A. (1992) Structural chemistry of Mn, Fe Co, and Ni in Mn hydrous oxides. I. Information from XANES spectroscopy. *Am. Mineral.* **77**, 1133–1143.
- Manceau A. and Gallup L. D. (2005) Nanometer-sized divalent manganese-hydrous silicate domains in geothermal brine precipitates. *Am. Mineral.* **90**, 371–381.
- Manceau A., Marcus A. M. and Grangeon S. (2012) Determination of Mn valence states in mixed-valent manganates by XANES spectroscopy. *Am. Mineral.* **97**, 816–827.
- Maynard J. B. (2010) The chemistry of manganese ores through time: a signal of increasing diversity of earth-surface environments. *Econ. Geol.* **105**, 535–552.
- McKeown D. A., Kot W. K., Gan H. and Pegg I. L. (2003) X-ray absorption studies of manganese valence and local environment in borosilicate waste glasses. *J. Non-Cryst. Solids* **328**, 71–89.
- Metcalfe I. (2006) Palaeozoic and Mesozoic tectonic evolution and palaeogeography of East Asian crustal fragments. The Korean Peninsula in context. *Gondwana Res.* **9**, 24–46.
- Middelburg J. J., De Lange G. J. and van Der Weijden C. H. (1987) Manganese solubility control in marine pore waters. *Geochim. Cosmochim. Acta* **51**, 759–763.
- Morgan J. J. (2005) Kinetics of reaction between O₂ and Mn(II) species in aqueous solutions. *Geochim. Cosmochim. Acta* **69**, 35–48.
- Mucci A. (2004) The behavior of mixed Ca–Mn carbonates in water and seawater: controls of manganese concentrations in marine porewaters. *Aquat. Geochem.* **10**, 139–169.
- Murray J. W., Dillard J. G., Giovanoli R., Moers H. and Stumm W. (1985) Oxidation of Mn(II): initial mineralogy, oxidation state and ageing. *Geochim. Cosmochim. Acta* **49**, 463–470.
- Nakagawa M., Santosh M. and Maruyama S. (2009) Distribution and minerals assemblages of bedded manganese deposits in Shikoku, Southwest Japan: implications for accretion tectonics. *Gondwana Res.* **16**, 609–621.
- Nakagawa M., Santosh M. and Maruyama S. (2011) Manganese formations in the accretionary belts of Japan: implications for subduction–accretion process in active convergent margin. *J. Asian Earth Sci.* **42**, 208–222.
- Nakagawa M., Fukuoka M., Kakehi K., Kakiuchi G., Tamaki Y. and Taniguchi T. (2014) Caryophyllite and greenalite from the manganese deposits in Shikoku, Southwest Japan. *Clay Sci.* **18**, 79–86.
- Neumann T., Heiser U., Leosson M. A. and Kersten M. (2002) Early diagenetic processes during Mn-carbonate formation: evidence from the isotopic composition of authigenic Carhodochrosites of the Baltic Sea. *Geochim. Cosmochim. Acta* **66**, 867–879.
- Oldham V. E., Owings S. M., Jones M. R., Tebo B. M. and Luther G. W. (2015) Evidence for the presence of strong Mn(III)-binding ligands in the water column. *Mar. Chem.* **171**, 58–66.
- Oldham V. E., Mucci A., Tebo B. M. and Luther G. W. (2017) Soluble Mn(III)-L complexes are abundant in oxygenated waters and stabilized by humic ligands. *Geochim. Cosmochim. Acta* **199**, 238–246.
- Okita P. M., Maynard J. B., Spiker E. C. and Force E. R. (1988) Isotopic evidence for organic matter oxidation by manganese reduction in the formation of stratiform manganese carbonate ore. *Geochim. Cosmochim. Acta* **52**, 2679–2685.
- Okita P. M. (1992) Manganese carbonate mineralization in the Molango District, Mexico. *Econ. Geol.* **87**, 1345–1366.
- Ossa O. F., Hofmann A., Vidal O., Kramers J. D., Belyanin G. and Cavalazzi B. (2016) Unusual manganese enrichment in the Mesoarchean Mozaan Group, Pongola Supergroup, South Africa. *Precambrian Res.* **281**, 414–433.
- Ostrander C. M., Nielsen S. G., Owens J. D., Kendall B., Gordon G. W., Romaniello S. J. and Anbar A. D. (2019) Fully oxygenated water columns over continental shelves before the Great Oxidation Event. *Nat. Geosci.* **12**, 186–191.
- Parker D. L., Takami M., Mylene L., Mozafarzadeh R. V., McCarthy J. K. and Tebo B. M. (2007) Inter-relationships of MnO₂ precipitation, siderophore–Mn(III) complex formation, siderophore degradation, and iron limitation in Mn(II)-oxidizing bacterial cultures. *Geochim. Cosmochim. Acta* **71**, 5672–5683.
- Planavsky N. J., McGoldrick P., Scott C. T., Li C., Reinhard C. T., Kelly A. E., Chu X., Bekker A., Love G. D. and Lyons T. W. (2011) Widespread iron-rich conditions in the mid-Proterozoic ocean. *Nature* **477**, 448–451.
- Planavsky N. J., Asael D., Hofmann A., Reinhard C. T., Lalonde S. V., Knudsen A., Wang X., Ossa O. F., Pecoits E., Smith A. J. B., Beukes N. J., Bekker A., Johnson T. M., Konhauser K. O., Lyons T. W. and Rouxel O. J. (2014) Evidence for oxygenic photosynthesis half a billion years before the Great Oxidation Event. *Nat. Geosci.* **7**, 283–286.
- Planavsky N. J., Crowe S. A., Fakrae M., Beaty B., Reinhard C. T., Mills B. J. W., Holstege C. and Konhauser K. O. (2021) The evolution of the size and scope of Earth's biosphere. *Nat. Rev. Earth Environ.* **2**, 123–139.
- Post J. E. (1999) Manganese oxide minerals: crystal structures and economic and environmental significance. *Proc. Natl. Acad. Sci.* **96**, 3447–3454.
- Poulton S. W. and Canfield D. E. (2011) Ferruginous conditions: a dominant feature of the ocean through Earth's history. *Elements* **7**, 107–112.
- Rasmussen B., Meier D. B., Krapež B. and Muhling J. R. (2013) Iron silicate microgranules as precursor sediments to 2.5-billion-year-old banded iron formations. *Geology* **41**, 435–438.
- Rasmussen B., Krapež B., Muhling J. R. and Suvorova A. (2015) Precipitation of iron silicate nanoparticles in early Precambrian oceans marks Earth's first iron age. *Geology* **43**, 303–306.
- Rasmussen B., Muhling J. R., Suvorova A. and Krapež B. (2017) Greenalite precipitation linked to the deposition of banded iron formations downslope from a late Archaean carbonate platform. *Precambrian Res.* **290**, 49–62.
- Ravel B. and Newville M. (2005) ATHENA, ARTEMIS, HEPHAESTUS: data analysis for X-ray absorption spectroscopy using IFEFFIT. *J. Synchrotron Radiat.* **12**, 537–541.
- Reinhard C. T., Planavsky N. J., Robbins L. J., Partin C. A., Gill B. C., Lalonde S. V., Bekker A., Konhauser K. O. and Lyons T. W. (2013) Proterozoic ocean redox and biogeochemical stasis. *Proc. Natl. Acad. Sci.* **110**, 5357–5362.
- Robbins L. J., Funk S. P., Flynn S. L., Warchola T. J., Li Z. Q., Lalonde S. V., Rostron B. J., Smith A. J. B., Beukes N. J., Kock M. O., Heaman L. M., Alessi D. S. and Konhauser K. O. (2019) Hydrogeological constraints on the formation of Palaeoproterozoic banded iron formations. *Nat. Geosci.* **12**, 558–563.
- Robie R. A., Huebner J. S. and Hemingway B. S. (1995) Heat capacities and thermodynamic properties of braunite (Mn₇SiO₁₂) and rhodonite (MnSiO₃). *Am. Mineral.* **80**, 560–575.
- Roy S. (2000) Late Archean initiation of manganese metallogenesis: its significance and environmental controls. *Ore Geol. Rev.* **17**, 179–198.
- Roy S. (2006) Sedimentary manganese metallogenesis in response to the evolution of the Earth system. *Earth Sci. Rev.* **77**, 273–305.
- Schieber J., Southard J. and Thaisen K. (2007) Accretion of mudstone beds from migrating floccule ripples. *Science* **318**, 1760–1763.

- Schulze D. G., Sutton S. R. and Bajt S. (1995) Determining Manganese Oxidation State in Soils Using X-ray Absorption Near-Edge Structure (XANES) Spectroscopy. *Soil Sci. Soc. Am. J.* **59**, 1540–1548.
- Sørensen J., Jørgensen K. S., Colley S., Hydes D. J., Thompson J. and Wilson T. R. S. (1987) Depth localization of denitrification in a deep-sea sediment from the Madeira Abyssal Plain. *Limnol. Oceanogr.* **32**, 758–762.
- Sun Y. D., Lai X. L., Wignall P. B., Widdowson M., Ali J. R., Jiang H. S., Wang W., Yan C. B., Bond D. P. and Védrine S. (2010) Dating the onset and nature of the middle Permian Emeishan large igneous province eruptions in SW China using conodont biostratigraphy and its bearing on mantle plume uplift models. *Lithos* **119**, 20–33.
- Tebo B. M., Bargar J. R., Clement B. G., Dick G. J., Murray K. J., Parker D., Verity R. and Webb S. M. (2004) Biogenic manganese oxides: properties and mechanisms of formation. *Annu. Rev. Earth Planet. Sci.* **32**, 287–328.
- Tebo B. M., Johnson H. A., McCarthy J. K. and Templeton A. S. (2005) Geomicrobiology of manganese(II) oxidation. *Trends Microbiol.* **13**, 421–428.
- Trouwborst R. E., Clement B. G., Tebo B. M., Glazer B. T. and Luther G. W. (2006) Soluble Mn(III) in suboxic zones. *Science* **313**, 1955–1957.
- Tsikos H., Beukes N. J., Moore J. M. and Harris C. (2003) Deposition, Diagenesis, and Secondary Enrichment of Metals in the Paleoproterozoic Hotazel Iron Formation, Kalahari Manganese Field, South Africa. *Econ. Geol. Bull. Soc. Econ. Geol.* **98**, 1449–1462.
- Urban H., Stribny B. and Lippolt H. J. (1992) Iron and manganese deposits of the Urucum District, Mato Grosso do Sul, Brazil. *Econ. Geol.* **87**, 1375–1392.
- Van Cappellen P. and Wang Y. (1996) Cycling of iron and manganese in surface sediments; a general theory for the coupled transport and reaction of carbon, oxygen, nitrogen, sulfur, iron, and manganese. *Am. J. Sci.* **296**, 197–243.
- Webb S. M., Dick G. J., Bargar J. R. and Tebo B. M. (2005) Evidence for the presence of Mn(III) intermediates in the bacterial oxidation of Mn(II). *Proc. Natl. Acad. Sci.* **102**, 5558–5563.
- Wei H. Y., Wei X. M., Qiu Z., Song H. Y. and Shi G. (2016) Redox conditions across the G-L boundary in South China: Evidence from pyrite morphology and sulfur isotopic compositions. *Chem. Geol.* **440**, 1–14.
- Wittkop C., Swanner E. D., Grengs A., Lambrecht N., Fakhraee M., Myrbo A., Bray A. W., Poulton S. W. and Katsev S. (2020) Evaluating a primary carbonate pathway for manganese enrichments in reducing environments. *Earth Planet. Sci. Lett.* **538** 116201.
- Xiao S. H., Schiffbauer J. D., McFadden K. A. and Hunter J. (2010) Petrographic and SIMS pyrite sulfur isotope analyses of Ediacaran chert nodules: Implications for microbial processes in pyrite rim formation, silicification, and exceptional fossil preservation. *Earth Planet. Sci. Lett.* **297**, 481–495.
- Xu H., Gao J. B., Yang R. D., Feng K. N., Wang L. B. and Chen J. (2021) Metallogenic mechanism of large manganese deposits from Permian manganese ore belt in western South China Block: New mineralogical and geochemical evidence. *Ore Geol. Rev.* **132** 103993.
- Yakushev E. V., Pollehne F., Jost G., Kuznetsov I., Schneider B. and Umlauf L. (2007) Analysis of the water column oxic/anoxic interface in the Black and Baltic seas with a numerical model. *Mar. Chem.* **107**, 388–410.
- Yakushev E., Pakhomova S., Sørensen K. and Skei J. (2009) Importance of the different manganese species in the formation of water column redox zones: observations and modeling. *Mar. Chem.* **117**, 59–70.
- Yan D. T., Zhang L. Q. and Qiu Z. (2013) Carbon and sulfur isotopic fluctuations associated with the end-Guadalupian mass extinction in South China. *Gondwana Res.* **24**, 1276–1282.
- Yan H., Pi D. H., Jiang S. Y., Hao W. D., Mänd K., Robbins L. J., Li L. and Konhauser K. O. (2020a) New constraints on the onset age of the Emeishan LIP volcanism and implications for the Guadalupian mass extinction. *Lithos* **360**, 1–14.
- Yan H., Pi D. H., Jiang S. Y., Hao W. D., Cui H., Robbins L. J., Mänd K., Li L., Planavsky J. N. and Konhauser K. O. (2020b) Hydrothermally induced ³⁴S enrichment in pyrite as an alternative explanation of the Late-Devonian sulfur isotope excursion in South China. *Geochim. Cosmochim. Acta* **283**, 1–21.
- Yang J. H., Cawood P. A., Du Y. S., Huang H. and Hu L. S. (2012) Detrital record of indosinian mountain building in SW china: provenance of the middle triassic turbidites in the youjiang basin. *Tectonophysics* **574**, 105–117.
- Zegeye A., Bonneville S., Benning L. G., Sturm A. and Fowle D. A. (2012) Green rust formation controls nutrient availability in a ferruginous water column. *Geology* **40**, 599–602.
- Zeng Y. F., Zhang J. Q., Liu W. J., Zhou H. L., Chen H. D., Xu X. H., Mao X. D. and Yang D. L. (1993) *Devonian lithofacies Paleogeography and mineralization in south China: Beijing*. Geological Publishing House, pp. 43–45, [in Chinese with English abstract].
- Zeng Y. Y. and Liu T. B. (1999) Characteristics of the Devonian Xialei manganese deposit, Guangxi Zhuang Autonomous Region, China. *Ore Geol. Rev.* **15**, 153–163.
- Zhang B. L., Wang C. L., Robbins L. J., Zhang L. C., Konhauser K. O., Dong Z. G., Peng Z. D. and Zheng M. T. (2020) Petrography and geochemistry of the Carboniferous Ortokarnash manganese deposit in the western Kunlun Mountains of Xinjiang Province, China: implications for the depositional environment and the origin of mineralization. *Econ. Geol.* **115**, 1559–1588.
- Zhang L. L., Yan S., Jiang S., Yang K., Wang H., He S. M. and Liang D. X. (2015) Hard X-ray micro-focusing beamline at SSRF. *Nucl. Sci. Tech.* **26** 060101.
- Zhang R. X. and Yang S. Y. (2016) A mathematical model for determining carbon coating thickness and its application in electron probe microanalysis. *Microsc. Microanal.* **22**, 1374–1380.
- Zhu B., Guo Z. J., Zhang S. N., Ukstins I., Du W. and Liu R. C. (2019) What triggered the early-stage eruption of the Emeishan large igneous province? *Geol. Soc. Am. Bull.* **131**, 1837–1856.